Prepared for submission to JCAP

Simulated Milky Way analogues: implications for dark matter indirect searches

Francesca Calore,[a] **Nassim Bozorgnia,**[a] **Mark Lovell,**[a,b] **Gianfranco Bertone,**[a] **Matthieu Schaller,**[c] **Carlos S. Frenk,**[c] **Robert A. Crain,**[d] **Joop Schaye,**[e] **Tom Theuns**[c] **& James W. Trayford**[c]

[a]GRAPPA, University of Amsterdam, Science Park 904, 1090 GL Amsterdam, Netherlands
[b]Instituut-Lorentz for Theoretical Physics, Niels Bohrweg 2, NL-2333 CA Leiden, Netherlands
[c]Institute for Computational Cosmology, Durham University, South Road, Durham DH1 3LE, UK
[d]Astrophysics Research Institute, Liverpool John Moores University, 146 Brownlow Hill, Liverpool L3 5RF, UK
[e]Leiden Observatory, Leiden University, PO Box 9513, NL-2300 RA Leiden, Netherlands

E-mail: f.calore@uva.nl

Abstract. We study high-resolution hydrodynamic simulations of Milky Way type galaxies obtained within the "Evolution and Assembly of GaLaxies and their Environments" (EAGLE) project, and identify those that best satisfy observational constraints on the Milky Way total stellar mass, rotation curve, and galaxy shape. Contrary to mock galaxies selected on the basis of their total virial mass, the Milky Way analogues so identified consistently exhibit very similar dark matter profiles inside the solar circle, therefore enabling more accurate predictions for indirect dark matter searches. We find in particular that high resolution simulated haloes satisfying observational constraints exhibit, within the inner few kiloparsecs, dark matter profiles shallower than those required to explain the so-called *Fermi GeV excess* via dark matter annihilation.

Contents

1 Introduction

Discovering the nature of dark matter (DM) is one of the main challenges for physics today. We have evidence of the DM gravitational interactions at different scales, from galactic up to cosmological scales (see e.g. [1–4]), but its nature remains a mystery. Weakly Interacting Massive Particles (WIMPs) are among the most well-motivated DM particle candidates, and they are currently searched for with three detection strategies: (a) *direct* detection, based on the measurement of the recoil energy of nuclei hit by DM particles in underground experiments, (b) *indirect detection*, through the search for secondary particles produced in the annihilation or decay of DM, and (c) the search for new particles beyond the standard model of particle physics at accelerators, in particular at the Large Hadron Collider.

The prospects for discovering DM particles with direct and indirect searches strongly depend on the distribution of DM in the Milky Way (MW). Recently an extensive compilation of measurements of the Milky Way rotation curve – i.e. of the circular velocity of astrophysical tracers as a function of the distance from the Galactic centre (GC) – has confirmed the existence of large amounts of DM within the solar circle [5], and enabled researchers to estimate the DM spatial density profile with parametric [6] and non-parametric methods [7, 8].

The DM density profile, $\rho(R)$ (where R is the distance from the GC), is a crucial ingredient for predicting the intensity flux and anisotropy of gamma rays produced by the annihilation of WIMPs in the halo of the MW, since the annihilation rate depends on the square of the DM particle number density. While the DM density profile at galactocentric distances $R > 5-6$ kpc is relatively well constrained by the analysis of kinematical data of the MW rotation curve, the DM profile in the inner few kiloparsecs from the GC is subject to large uncertainties [7]. In the absence of observational constraints, the most profitable recourse is examination of N-body, and, more recently, hydrodynamic simulations. Pure DM

N-body simulations predict a DM density profile that behaves like $r^{-\gamma}$, where $\gamma \approx 1$ in the few inner kiloparsecs, as encoded in the so-called Navarro-Frenk-White (NFW) profile [9]. Baryonic processes can either lower or increase the DM density in the inner halo [10–16]. However, the size of those effects is still a matter of debate.

In a recent exciting development for indirect dark matter searches, an unexplained excess of gamma rays collected with the Large Area Telescope (LAT) – aboard the *Fermi* satellite – from the centre of our Galaxy has been discovered over and above the standard adopted astrophysical background [17–26]. In particular, ref. [25] re-assessed the spectral and morphological properties of the GeV excess, taking into account background model systematics associated with the Galactic diffuse emission modelling. The striking similarity of the observed gamma-ray excess with the signal predicted from the annihilation of DM particles in the halo of the MW makes the DM interpretation very appealing (see e.g. [23, 24, 27, 28]), although other viable astrophysical explanations have been put forward [29–37].

Among the alternative GeV excess sources, the possibility that the excess originates from a series of leptonic outbursts which occurred $\sim 0.1 - 1$ yr ago has recently been demonstrated to be a viable scenario but a quite unlikely one [36] given the set of parameters needed to fully account for the spectral *and* morphological properties of the GeV excess emission. On the other hand, the vigorously debated interpretation in terms of the unresolved emission from very dim sources, such as for example pulsars [33] and milli-second pulsars [29–32], has been very recently corroborated by two independent works [38, 39]. While it is clear that the disc population of unresolved pulsars and milli-second pulsars cannot contribute more than 10% to the excess emission [40], the contribution from a new population associated with the Galactic bulge seems instead to be sufficient to explain the full signal [38, 39].

Given the lively debate on possible explanations, and the difficulty of firmly confirming or refuting them, it is crucial to fully exploit state of the art simulations to examine what is the expected DM profile of MW-like galaxies, in order to refine predictions for the DM annihilation gamma-ray flux. We will therefore compare the predictions from the set of selected MW-like galaxies with the GeV excess gamma-ray measurements.

In this work, we study the distribution of DM in MW-like galaxies simulated within the EAGLE project [41, 42] – a suite of cosmological, hydrodynamic simulations calibrated to reproduce the observed distribution of stellar masses and sizes of low-redshift galaxies and designed to address many outstanding issues in galaxy formation such as metallicities of galaxies, properties of the intergalactic medium and the effect of feedback on scales ranging from dwarf galaxies up to giant ellipticals. We consider at first all galaxies within haloes with virial mass in the range $\mathcal{O}(10^{12} - 10^{14})\,\mathrm{M}_\odot$, and we post-process this sample of MW analogues by requiring that they satisfy observational constraints on the Galactic rotation curve [5], the total stellar mass and the presence of a dominant disc in the stellar component.

We then evaluate the DM density profile of the final set of what we define to be *MW-like galaxies* and discuss the prospects for DM indirect detection (the implications for direct detection will be discussed in an upcoming paper [43]). In particular, we discuss the implications of the resulting DM density profiles for the DM interpretation of the *Fermi* GeV excess.

After presenting the set of cosmological hydrodynamic simulations used in section 2, we will describe our selection procedure and derive the set of MW-like galaxies in our samples in section 3. We will dedicate section 4 to the analysis of the DM density profiles of the set

Name	L (Mpc)	N	$m_{\rm g}$ (M$_\odot$)	$m_{\rm dm}$ (M$_\odot$)	ϵ (pc)
EAGLE HR	25	2×752^3	2.26×10^5	1.21×10^6	350
EAGLE IR	100	2×1504^3	1.81×10^6	9.70×10^6	700
APOSTLE IR	–	–	1.3×10^5	5.9×10^5	308
APOSTLE HR (I)	–	–	1.0×10^4	5.0×10^4	134
APOSTLE HR (II)	–	–	5.0×10^3	2.5×10^4	134

Table 1. Parameters of the simulations discussed in this paper. L is the comoving sidelength of the simulation cube, N the number of simulation particles prior to splitting, $m_{\rm g}$ the initial gas particle mass, $m_{\rm dm}$ the DM particle mass, and ϵ the Plummer-equivalent physical softening length. The resolution limit is usually taken to be $2.8\times\epsilon$, i.e. 1.96, 0.98 and 0.87 kpc for EAGLE IR, EAGLE HR and APOSTLE IR, respectively.

of MW-like galaxies and finally section 5 to the discussion of the implications for the GeV excess emission. We conclude in section 6. Appendices A and B contain additional material supporting our findings.

2 Simulations

In this section we briefly describe the set of simulations used, which form part of the EAGLE project [41, 42]. The EAGLE simulations were performed using a modified version of the P-GADGET3 Tree-Smoothed Particle Hydrodynamics (SPH) code [44] that has been modified to use the state-of-the-art SPH flavour of [45] (whose impact on the galaxy population is discussed by [46]). The cosmological parameters were chosen to be those derived from the analysis of the *Planck* 2013 measurements [47] and they have the following values: $\Omega_m = 0.307$, $\Omega_\Lambda = 0.693$, $\Omega_b = 0.0482$, $h = 0.678$, $\sigma_8 = 0.83$, and $n_s = 0.961$. The simulations were run at two different resolutions, which we refer to as intermediate (EAGLE IR) and high resolution (EAGLE HR). The former was run in a series of cosmological volumes up to a maximum of 100 Mpc on one side, and the latter up to 25 Mpc. The simulations start at z=127 with an equal number of gas and DM particles whose masses are given in table 1. Gas particles have a finite probability to be turned into star particles that increases with the gas pressure, such that the local star formation law [48] is reproduced. Each star particle represents a simple stellar population, and inherits the mass and element abundances of the parent gas particle. The properties of the two EAGLE runs used in this study (EAGLE IR and EAGLE HR) are reproduced from [41] in table 1. In addition to the EAGLE cosmological volumes, we also make use of simulations of the APOSTLE project [49, 50]. These simulations use the same code as the EAGLE project applied to zoomed regions containing a close pair of $\sim 10^{12}$M$_\odot$ DM haloes that could host our MW galaxy and M31, i.e. be an analogue of the Local Group. We use twelve APOSTLE volumes simulated at similar resolution to EAGLE HR, which as a group we denote APOSTLE IR (for "intermediate" resolution). In addition, APOSTLE consists of other two re-simulations at ten times higher mass resolution, denoted generically as APOSTLE HR. Their simulation details are also included in table 1. One minor difference from the EAGLE cosmological volumes is that they use the WMAP-7 cosmological parameters: $\Omega_m = 0.272$, $\Omega_\Lambda = 0.728$, $\Omega_b = 0.0455$, $h = 0.704$, $\sigma_8 = 0.81$, and $n_s = 0.967$.

To select MW-like galaxy candidates, we first extract all galaxies located at the minimum of their halo potential wells as returned by the SUBFIND algorithm [51] (i.e. we exclude satellite galaxies) in haloes of virial mass, M_{200}, in the range $5 \times 10^{11} < M_{200}/\mathrm{M}_\odot < 1 \times 10^{14}$, where M_{200} is defined as the mass enclosed within the sphere that contains a mean density 200 times the critical density. We extend our range to the most massive haloes because the model underpredicts slightly the stellar masses contained within haloes of $M_{200} \sim 10^{12}\mathrm{M}_\odot$ [41], and therefore MW mass galaxies are found in haloes that are slightly more massive than is inferred from abundance matching results, e.g. [52]. We show in appendix A that this mismatch between halo mass and stellar mass has little effect on our results.[1]

3 Selection of Milky Way-like galaxies

We consider the simulation runs EAGLE IR, EAGLE HR and APOSTLE IR described in section 2. We start from the corresponding subsets of galaxies at the centre of haloes with $5 \times 10^{11} < M_{200}/\mathrm{M}_\odot < 1 \times 10^{14}$. The initial sets are composed of 2411, 61 and 24 objects for the EAGLE IR, EAGLE HR and APOSTLE IR run, respectively.

In this section we aim to select the galaxies that most closely resemble the MW. Our definition of MW-like galaxies is based on a minimal set of criteria that the simulated haloes should satisfy. In particular, for a simulated halo to host a good MW-like galaxy, we require that:

(i) The simulated rotation curve fits well the observed MW kinematical data in ref. [5]. We explain the method followed to derive the rotation curves from the simulation, the data used in the analysis and the goodness of fit definition in section 3.1.

(ii) The total stellar mass of the simulated galaxies is within the 3σ MW range derived from observations, $4.5 \times 10^{10} < M_*/\mathrm{M}_\odot < 8.3 \times 10^{10}$ [53]: 335, 12, and 2 galaxies satisfy this constraint in the EAGLE IR, EAGLE HR and APOSTLE IR run respectively.[2]

(iii) The galaxies contain a substantial stellar disc component. See section 3.2.

The three criteria listed above define our MW-like galaxies. The final sets of *good* objects are presented in section 3 for the EAGLE IR, EAGLE HR and APOSTLE IR simulations.

We are aware of the fact that besides structural parameters, such as the rotation curve used in the present work, more criteria should be imposed to identify truly MW-like galaxies, such as brightness profile constraints, star formation history, metallicity gradient, and disc scale length/height. However, we stress that our main purpose is to derive implications for indirect DM searches rather than to test the ability of the EAGLE simulation code to reproduce the MW. Indirect detection prospects depend on the shape of the DM profile, which turns out to be almost universal for the simulated objects in EAGLE IR, EAGLE HR and APOSTLE IR as shown in ref. [54] and more thoroughly in section 4. The method presented here is general and can be applied to future simulations.

3.1 Observed Milky Way rotation curve and goodness of fit

Recently, ref. [5] collated a large amount of observational measurements of the MW rotation curve and compared these with the expectations from a large set of baryonic models, finding

---

[1] Appendices refer to the EAGLE set of simulations. However, the conclusions reached there can be safely extended to the APOSTLE IR run.

[2] We note that for APOSTLE IR one of the two galaxies falls on the lower boundary of the 3σ observed range. In order to have more than one galaxy in the final selection, we keep this one as well.

robust evidence for DM even within the inner 5 – 6 kpc of the Galaxy. We make use of the recent compilation of kinematic tracers presented in [5]. We adopt a local circular velocity of $v_0 = 230$ km/s, a local galactocentric distance of $R_0 = 8$ kpc, and the component of the solar peculiar velocity in the direction of the Galactic rotation, $V_\odot = 12.24$ km/s [55], as fiducial values for the analysis presented below. However, owing to the thorough discussion by [5] about the uncertainty in the rotation curve data due to v_0 and R_0, we dedicate appendix B to the scrutiny of possible variations in the results due to different choices of v_0 and R_0 and we show that our main conclusions remain unchanged.

The observational data are provided as constraints on the angular circular velocity, $\omega_c(R) = v_c(R)/R$, and the galactocentric distance R. Here $v_c(R)$ is the circular velocity at distance R. As explained by [5], using the angular circular velocity for fitting purposes is more convenient than working with $v_c(R)$, since the errors of $\omega_c(R)$ and R are not correlated, while this is not the case for $v_c(R)$ and R.

The circular velocity, $v_c(R)$, is defined as the velocity of a test particle on a circular orbit at radius R from the GC. By equating the centripetal and gravitational forces on the test particle, it is simple to show that, for a spherically symmetric matter distribution:

$$v_c(R) = \sqrt{\frac{GM(<R)}{R}}\,, \tag{3.1}$$

where $M(< R)$ is the total mass enclosed within radius R, and G is the universal gravitational constant. In figure 1, we display the kinematical data in the plane (ω_c, R) together with the rotation curves predicted by *all* haloes in the EAGLE IR (top left panel), EAGLE HR (top right panel), and APOSTLE IR (bottom panel) simulation runs, satisfying our halo mass constraint. From figure 1, it is evident that there is a wide range of variation in the rotation curves from the simulation when considering all objects whose halo mass, M_{200}, lies in the selected MW mass range, $5 \times 10^{11} < M_{200}/\mathrm{M}_\odot < 1 \times 10^{14}$. However, by forcing the haloes to have the correct total stellar mass (in the 3σ observed range for the MW), the number of good objects is reduced significantly: from 2411 to 335 for EAGLE IR, from 61 to 12 for EAGLE HR, and from 24 to 2 for APOSTLE IR. We also display the haloes that give the best fit to the kinematical data (see below for further details). Therefore, classifying a halo with the correct halo mass as MW-like is too simplistic a criterion, and thus will often fail to reproduce the MW kinematical data. For this reason, we extend the definition of MW-like galaxies to account for the agreement with the observed Galactic rotation curve.[3]

To derive the goodness of fit of the simulated rotation curve to the observed data, it is convenient to work with the reduced quantities $x \equiv R/R_0$ and $y \equiv \omega_c/\omega_0 - 1$ [5], where $\omega_0 \equiv v_0/R_0$. The two-variable χ^2 can be written as:

$$\chi^2 = \sum_i \frac{(y_i - \hat{y}(x_i))^2}{\sigma_{y_i}^2 + (dy_i/dx_i)^2\,\sigma_{x_i}^2}\,, \tag{3.2}$$

---

[3] More realistically the requirement of spherical symmetry is not guaranteed to be a good approximation, and thus Equation 3.1 may not be appropriate. As a check, for the APOSTLE IR galaxies we calculated a series of rotation curves by summing up the gravitational forces due to all of the simulation particles in the box. We found that the difference in rotation curve amplitude between the full calculation and that obtained from the spherical symmetry is typically less than 10% at all radii. Moreover, we checked that the χ^2 values of these new rotation curves (for the fit to the measured MW rotation curve) are not significantly different from the ones obtained by assuming spherical symmetry. Most importantly, the ordering of haloes based on χ^2 values stays the same. We therefore conclude that our assumption of spherical symmetry is appropriate for this study.

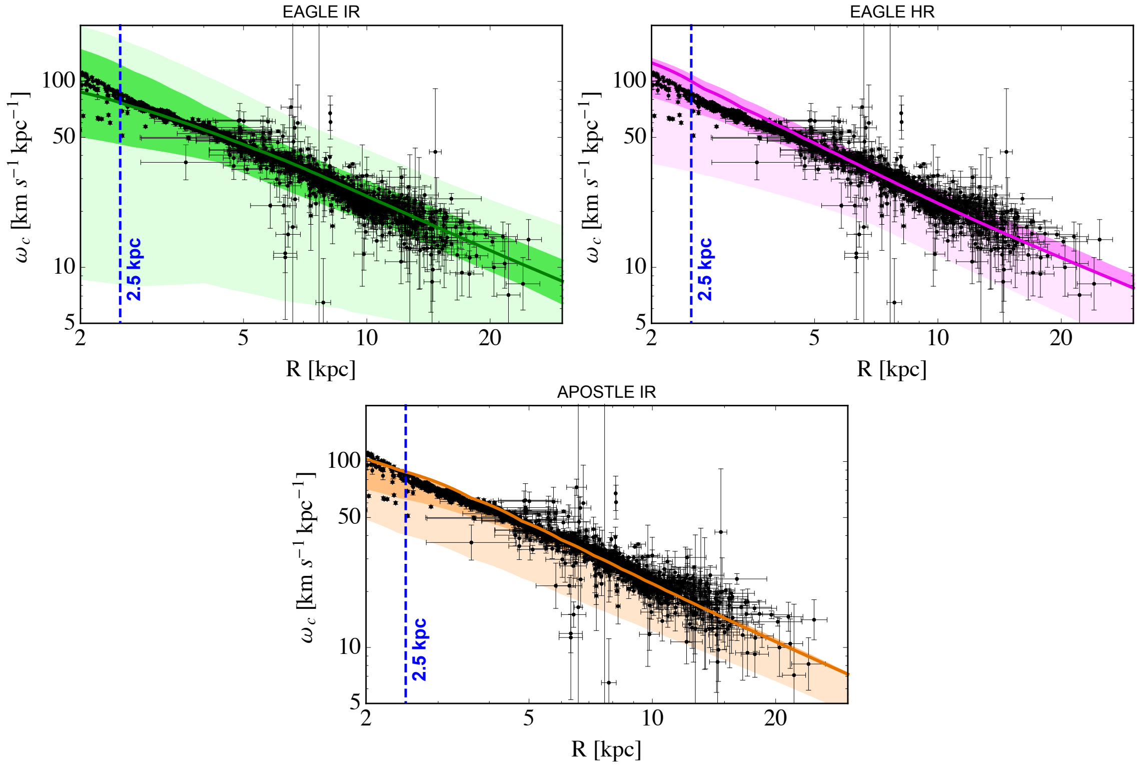

Figure 1. Kinematical data from [5] used in this work (*black* points and error bars) and rotation curves of simulated haloes for the EAGLE IR (*top left* panel), EAGLE HR (*top right* panel), and APOSTLE IR (*bottom centre* panel) runs. The *green*, *magenta*, and *orange* curves correspond to galaxies which fit our criteria as defined in section 3 and give the best fit (lowest χ^2 in eq. (3.2)) in the EAGLE IR, EAGLE HR, and APOSTLE IR runs, respectively. The *light* and *dark* coloured bands correspond to all simulated objects ($5 \times 10^{11} < M_{200}/\mathrm{M}_\odot < 1 \times 10^{14}$) and those which, in addition, satisfy the observed MW stellar mass range ($4.54 \times 10^{10} < M_*/\mathrm{M}_\odot < 8.32 \times 10^{10}$), respectively. The vertical *dashed blue* line marks the minimal radius considered in the fitting procedure (see text for further details).

where i runs over the observational data points considered, and $\hat{y}(x_i)$ is the simulated rotation curve evaluated at $x_i = R_i/R_0$. Both experimental errors in x (σ_{x_i}) and y (σ_{y_i}) are considered and obtained through standard error propagation from the errors in ω_c and R. For the fit, we consider measurements at $R > 2.5$ kpc. Indeed, the data derived by [5] assume circular orbits for the tracers and this approximation can break at small radii due to the effect of the Galactic bulge gravitational potential. Note also that 2.5 kpc is larger than the gravitational softening length used in our simulations.

In figure 2, we show the reduced χ^2 versus the total stellar mass, with N=2687 the total number of observational data points for the three sets of simulations. From the top left panel, which refers to EAGLE IR run, it is evident that the global minimum of the $\chi^2/(N-1)$ distribution naturally occurs within the 3σ measured range of the MW total stellar mass [53]. In other words, a good match of the simulation with the measured MW rotation curve is given by galaxies that have the correct MW stellar mass. In general, the contribution to rotation curves from stars (which largely dominate over the gas in the total

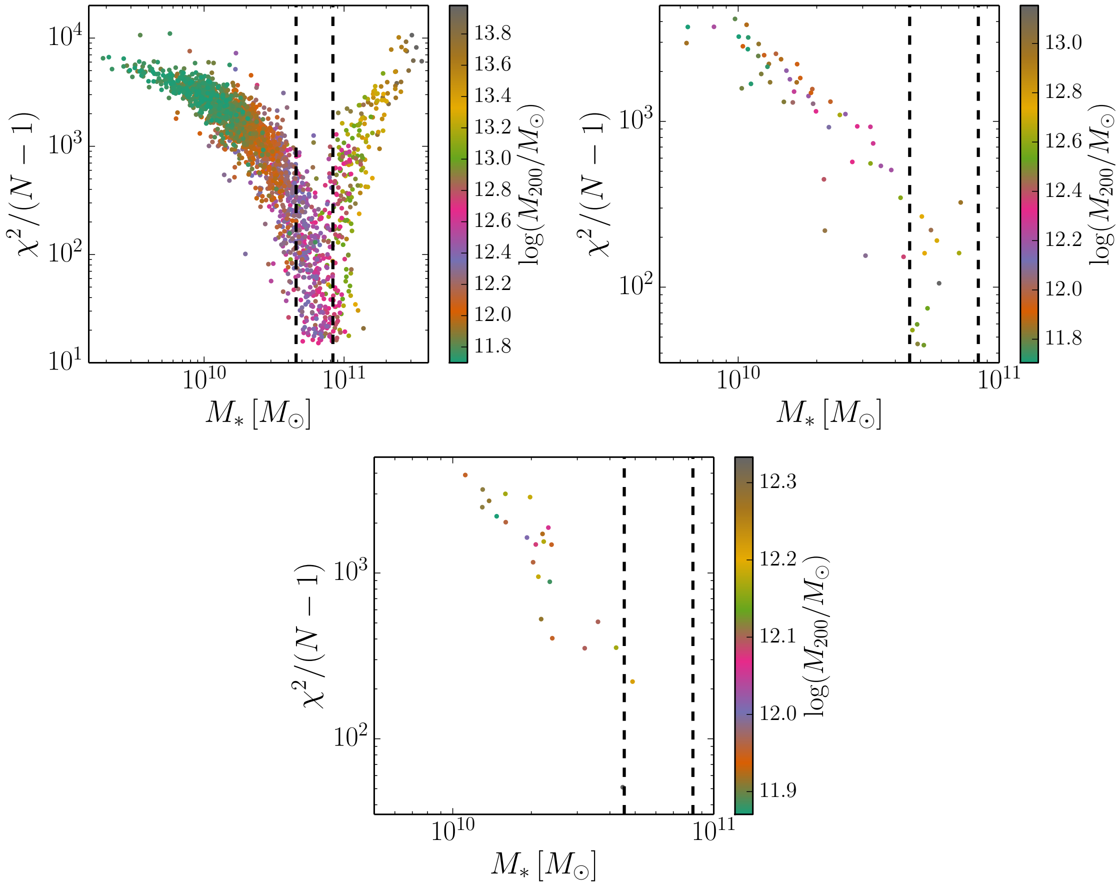

Figure 2. Reduced χ^2, $\chi^2/(N-1)$, versus total stellar mass for EAGLE IR (*top left* panel), EAGLE HR (*top right* panel) and APOSTLE IR (*bottom* panel). The *coloured* dots indicate the whole set of 2411, 61 and 24 simulated haloes in EAGLE IR, EAGLE HR and APOSTLE IR; of those, 335, 12 and 2 galaxies lie in the 3σ measured range (*black dashed* vertical lines) of the MW total stellar mass [53]. The colour-bar shows the distribution of halo mass, M_{200}.

baryonic component) is larger than the DM contribution up to $R \lesssim 5$ kpc. We note that by performing the analysis with a distance cut at 5 kpc our results remain unchanged.

The halo masses of the simulated galaxies with correct stellar mass and in the minimum reduced χ^2 region are larger than expected from observations of the MW, as for example $M_{200,\mathrm{MW}} = 1.2^{+0.7}_{-0.4} \times 10^{12}\,\mathrm{M}_\odot$ [56]. This result might indicate that the feedback in EAGLE simulated haloes in this mass range is slightly too efficient, and thus the stellar mass per unit halo is suppressed with respect to that inferred from estimates of the MW stellar and halo masses. This shortcoming is reflected in the stellar luminosity function, in that EAGLE underpredicts the abundance of galaxies with stellar masses $\sim 2-8\times10^{10} M_\odot$ relative to what is observed in galaxy surveys [41]. We also note that the total MW halo mass is affected by large uncertainties, with estimates based on kinematics of satellites, abundance matching, and the local Hubble flow, yielding somewhat discrepant results [57–60]. However, in appendix A, we show that the quantities relevant for DM indirect detection, and, in particular, for the implications on the GeV excess interpretation, are not affected by the large halo mass. We are thus confident that this mismatch between halo mass and stellar mass has little effect on

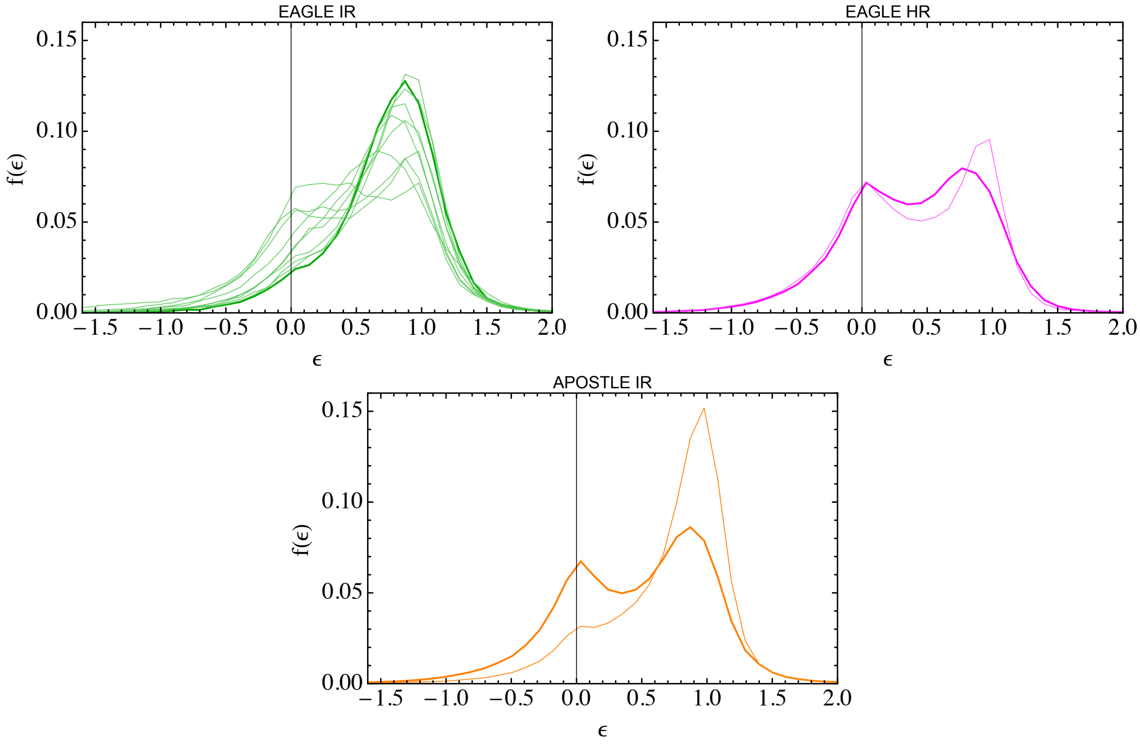

Figure 3. Distribution of stellar circularities, $f(\epsilon)$, for the haloes selected in the EAGLE IR (*top left* panel), EAGLE HR (*top right* panel), and APOSTLE IR (*bottom centre* panel) resolution runs according to our criteria, including the requirement of having a significant disc stellar component. *Thick* lines refer to the haloes giving the best-fit to the Galactic rotation curve for the three runs.

our final results.

3.2 Morphology of simulated galaxies: disc and spheroid

The MW is a spiral galaxy, with a well defined, unperturbed thin disc, a small bulge and a bar component. We therefore seek to select simulated galaxies that are themselves disc galaxies rather than ellipticals or undergoing mergers.

Following the approach of ref. [61], we characterise the dynamics of each simulated galaxy by looking for evidence of coherent rotation. Each star particle in the simulated galaxies possesses an angular momentum vector relative to its host's standard of rest. Any bulk stellar component that has the same angular momentum vector as that of the hosting simulated galaxy will be considered to belong to the disc. We can therefore use the distribution of angular momentum vectors of individual particles relative to the net angular momentum of the galaxy to discriminate between *discs* (coherent rotation) and *spheroids* (no coherent rotation; comprises bulges and stellar haloes).

For each selected galaxy, we derive the distribution of the stellar orbital circularity parameter, ϵ:

$$\epsilon(r) \equiv \frac{j_z}{j_c(r)} = \frac{j_z}{r v_c(r)}, \tag{3.3}$$

where j_z is the component of the specific angular momentum parallel to the total angular momentum of the galaxy, and $j_c(r)$ is the total specific angular momentum of a circular orbit

Name	$M_*[\times 10^{10}\,\mathrm{M}_\odot]$	$M_{200}[\times 10^{12}\,\mathrm{M}_\odot]$	D/T	$\chi^2/(N-1)$
EAGLE IR	6.69	4.38	0.70	16.56
	6.95	2.39	0.61	17.32
	7.16	9.12	0.69	17.59
	6.10	2.61	0.51	17.67
	7.91	6.28	0.52	18.23
	5.53	5.36	0.50	18.30
	6.78	2.33	0.60	18.47
	6.22	2.23	0.69	18.83
	5.50	3.09	0.65	18.84
	6.83	3.08	0.43	19.45
EAGLE HR	5.31	3.50	0.45	74.55
	5.48	2.76	0.46	220.96
APOSTLE IR	4.48	2.15	0.50	51.04
	4.88	1.68	0.70	221.27

Table 2. Relevant parameters of the finally selected MW-like galaxies that satisfy our selection criteria in the EAGLE IR, EAGLE HR and APOSTLE IR runs. We quote: total stellar mass, halo mass, disc-to-total mass ratio (D/T), and reduced χ^2 for the fit to the rotation curve data.

at distance r; here specific angular momentum is defined as angular momentum divided by the star particle mass. The distribution of stellar *circularities*, $f(\epsilon)$, is a good indicator of the relative importance of the disc with respect to the spheroidal stellar component. A disc in rotational support, that is a configuration in which gravitational collapse is offset by the centripetal acceleration, corresponds to a distribution peaked at about $\epsilon = 1$, while stars in a system supported by dispersion (i.e. a spheroidal system) show an almost symmetric distribution around $\epsilon = 0$ [61–63].

As a further constraint – in addition to the goodness of fit to the observed MW rotation curve – we want to select objects whose stellar kinematics shows a disc component and, thus, are not completely dominated by the spheroidal contribution. When building $f(\epsilon)$, we calculate the net specific angular momentum of the disc using only those star particles with galactocentric radii in the range 3 – 20 kpc. In this way, our determination of the disc angular momentum direction should neither be affected by the isotropic motions of bulge stars at low radii nor by high angular momentum halo stars at large radii. We inspect the distribution of stellar *circularities*, $f(\epsilon)$, for the haloes giving the best fit to the rotation curve data with the aim of building a final subset of objects that pass our criteria and can be considered to be MW-like in our perspective. We retain a galaxy if the stellar fraction in the range $\epsilon > 0.45$ is larger than 50%. This criterion is meant to identify galaxies that have a dominant disc and, on the other hand, to remove galaxies that show an almost symmetric distribution around $\epsilon = 0$ – and can thus be classified to have a spheroidal only component. We tested different cuts on $f(\epsilon)$ and adopted the one that is most conservative in retaining objects with a significant disc component. We note that the above criterion relies on the stellar kinematics only, and that it might differ from the bulge-to-disc decomposition given by photometric measurements. Indeed, photometric observations depend on assumptions on the shape of the brightness profile of the spheroidal and disc components [62, 64]. However, a full comparison of the simulation outcome and the photometry of the MW is beyond the scope of the present work and it would be interesting to study with follow-up analyses.

In the case of the EAGLE IR run the number of galaxies passing the stellar mass *and* disc dominance criteria is 145. Therefore, we further reduce the set of objects of the EAGLE IR resolution run by selecting those that have a reduced $\chi^2 < 20$ for the fit to the MW rotation curve data. For the EAGLE IR run, we thus finally select 10 MW-like galaxies. For the EAGLE HR resolution run, instead, we do not impose any further constraint on the χ^2, since only 2 objects survive the $f(\epsilon)$ criterion (and lie in the correct stellar mass range), due to the 64 times smaller simulation volume. Finally, for the APOSTLE IR run, the 2 galaxies satisfying the dynamical and stellar mass constraints also match the disc requirement.

In figure 3, we show the distribution of stellar fraction for the galaxies that give the best χ^2 to the rotation curve data, have the acceptable MW stellar mass, and show a substantial stellar fraction in the disc in the EAGLE IR, EAGLE HR, and APOSTLE IR runs. The reduced χ^2 values are quoted in table 2. We note that in the cases of the EAGLE HR and APOSTLE IR runs, the statistics for the initial sample are quite poor. In these cases the galaxy with the lowest χ^2 does not have any privileged statistical meaning, since the true minimum of the distribution is not guaranteed to have been found because of the small statistics. However, from the EAGLE IR results we are confident that the global minimum should lie within the correct MW stellar mass range. The fact that the χ^2 values of the EAGLE HR and APOSTLE IR runs are worse than the EAGLE IR one is thus not surprising. In what follows, we will use the best-fit galaxy as a reference for illustrating the implications for DM indirect detection.

For the sake of completeness, we also quote here the reduced χ^2 of the 4 galaxies belonging to the APOSTLE HR which are analysed in detail in ref. [65]. The reduced χ^2 values are (in order): 1203, 1982, 2056, 3554. Those are clearly poorer than the runs analysed in this work, but, again, the sample is very limited in number. Moreover, we have checked that those galaxies have a lower total stellar mass than what is observed within 3σ ($M_*/(10^{10}\,\mathrm{M}_\odot) = 2.22$, 1.56, 1.05, and 1.06, from smallest to largest χ^2 respectively). Since the stellar mass plays a role in the determination of rotation curves in the inner 5 kpc, such a discrepancy in the stellar mass can be a further reason for the poor χ^2.

To corroborate the implementation of criterion (iii), in figures 4, 5 and 6 we display the images of the edge-on and face-on orientations of the selected MW-like galaxies in the EAGLE IR, EAGLE HR and APOSTLE IR run. The images are produced with the radiative transfer code SKIRT [66]. This code generates images of the galaxy in the u, g, and r SDSS filters within a 30 kpc aperture of the galaxy centre; the dust distribution is inferred from the gas metal distribution in the interstellar medium [67, 68]. From those images one can see that the majority of the selected objects shows clearly a disc component.

To further test the prominence of the disc, we compute the disc-to-total mass ratio for the set of selected MW-like galaxies. The disc-to-total mass ratio writes as [61],

$$\frac{D}{T} \equiv \frac{M_d}{M_d + M_s}\,, \tag{3.4}$$

where $M_d = \sum_{\epsilon_i > 0.6} (f(\epsilon_i)\, m_g)$ is the stellar mass in the disc, and $M_s = \sum_{\epsilon_i > -0.6}^{\epsilon_i < 0.6} (f(\epsilon_i)\, m_g)$ is the stellar mass in the spheroid. The disc-to-total mass ratios are listed in table 2 for the sets of the selected MW analogues in the three simulations and are all in the range $0.4 - 0.7$. For the EAGLE HR simulation run, the ratios are systematically lower than what is expected for real spiral galaxies [69], while for some galaxies in the EAGLE IR and APOSTLE IR runs the D/T ratio is closer to observations of the MW, $(D/T)_{\mathrm{MW}} \sim 0.86$ [53].

In summary, we have identified a minimal set of 10, 2 and 2 galaxies for the EAGLE IR, EAGLE HR and APOSTLE IR simulation runs that simultaneously (i) give a good fit to the rotation curve of the MW, (ii) have the right total stellar mass (within 3σ) of the measured value, and (iii) show a significant disc stellar component. In table 2, we summarise the main properties of the chosen galaxies for the three simulation runs. These three subsets of objects represent MW analogues according to our definition. We have thus demonstrated that minimal selection criteria, such as the requirement to give a good fit to the observed rotation curve, significantly reduce the number of prototypical MW-like galaxies. In sections 4 and 5 we will use the two sets of galaxies to investigate the distribution of DM in the halo and discuss implications for indirect DM searches. We finally stress that discussing the matching of EAGLE simulated galaxies with other MW observables, such as the brightness emission profile, is beyond the scope of the present paper. Further studies along this direction would be extremely helpful for the field.

4 The Galactic dark matter density profile

In this section we analyse the DM density profile of the final set of MW-like galaxies and discuss possible implications for DM indirect detection. As explained in section 1, the predicted DM annihilation flux is very sensitive to the DM density profile and it is thus important to study the predictions of hydrodynamic simulations and any deviations from pure DM N-body simulation density profiles. As for the EAGLE simulations, it has been shown that, on average, haloes in the MW mass range ($\sim 10^{12}\mathrm{M}_\odot$) have a DM density profile that significantly deviates from the NFW profile and has a core in the inner few kiloparsecs [54]. Although the flattening might appear below the effective resolution (depending on the resolution run considered), the presence of a core on small radial distances from the GC seems to be a universal feature of EAGLE simulated objects. This has been recently demonstrated for the set of galaxies of the APOSTLE project, which were run with the same code and subgrid physics model as EAGLE; the density profile properties of the highest APOSTLE simulation run have been analysed in detail in [65]. We turn now to the analysis of the density profiles of our final set of MW-like galaxies.

In the left panels of figure 7, we show the DM density profile of the final set of haloes for the EAGLE IR, EAGLE HR and APOSTLE IR runs. The DM density is derived directly from the mass enclosed in a given shell between R and R + δR, adopting equally spaced radial bins in logarithmic space. By construction, we assume spherical symmetry for the distribution of DM, which has been shown to be a good assumption for the APOSTLE simulations [65]. Furthermore, it has been shown that baryons tend to make the distribution of DM more spherical than in simulations including solely DM [70–72]. We verified that for our set of MW-like galaxies the assumption of a spherically symmetric profile is a good approximation. The uncertainty in the density is given by the Poissonian error in the number of particles in each mass shell (the error in the distance refers instead to the adopted binning). As presented in section 2, the effective resolution limit of the simulation runs, i.e. the Plummer-equivalent softening length, is $2.8 \times \epsilon$, where $\epsilon = 0.7$ kpc, 0.35 kpc and 0.31 kpc for the EAGLE IR, EAGLE HR and APOSTLE IR runs, respectively. However, the radius at which profiles can be considered as converged is larger than this value and can be estimated in collisionless simulations using the criterion of [73] that identifies the radius at which the integral in mass is independent on the resolution. The so-called "Power radius" is $R_{\mathrm{P03}} =$

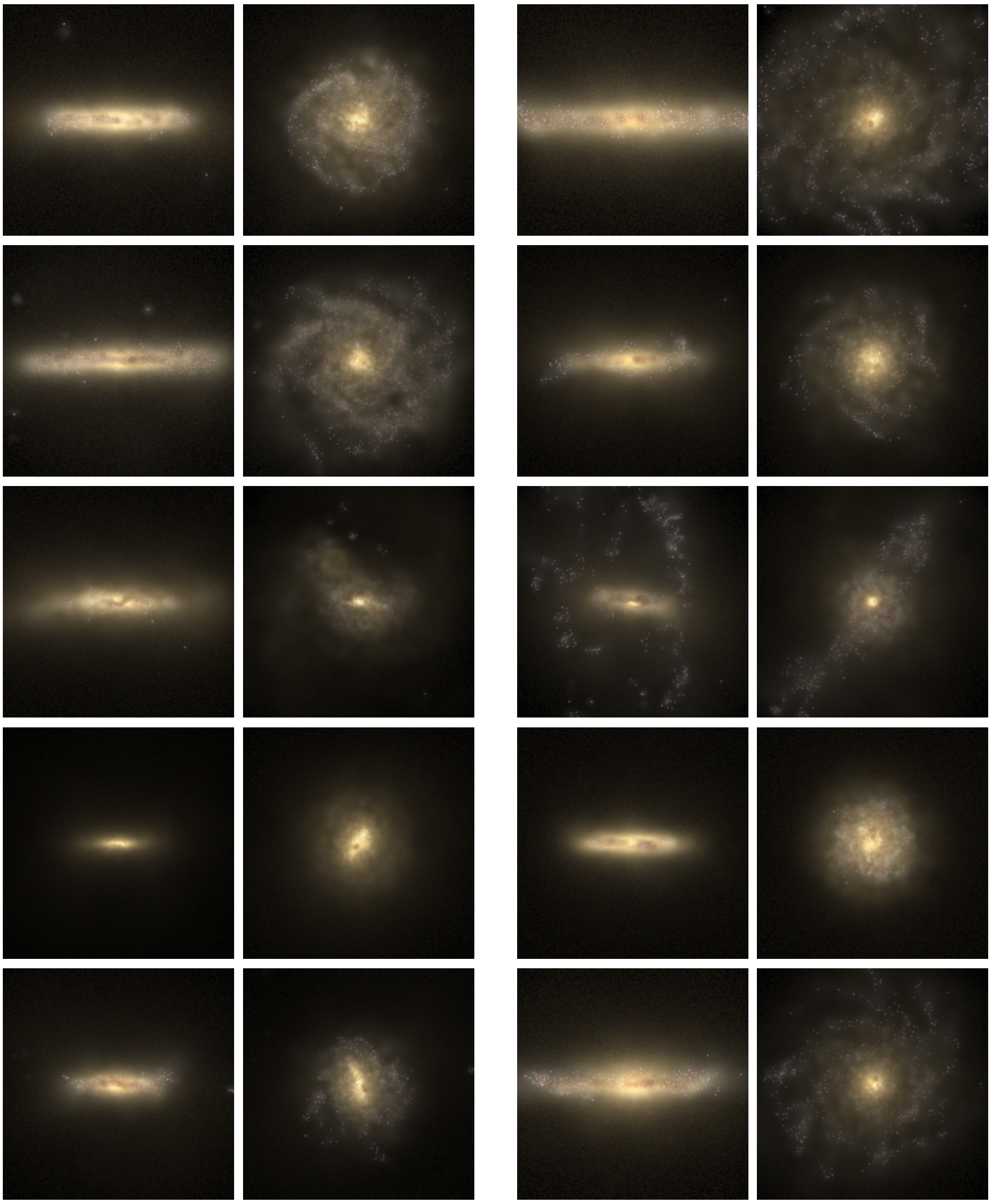

Figure 4. Pairs of mock three-colour composite grid observations for the 10 simulated galaxies in the EAGLE IR run with edge-on (*left*) and face-on (*right*) projections, within a 30 kpc aperture of the galaxy centre obtained using the SKIRT [66] radiative transfer code as described by [67, 68].

3.6 kpc, 1.8 kpc and 1.8 kpc[4] for the EAGLE IR, EAGLE HR and APOSTLE IR runs. The very concept of convergence – that ever increasing resolution will cause the measured quantity to asymptotically tend towards some finite value – is much less clear in simulations that

---

[4] The Power radius is a halo-dependent quantity and thus it is defined for each halo. We checked however that the variation of R_{P03} among haloes of the same simulation run varies only within a few percent. Therefore, using an average value for R_{P03} is a good approximation.

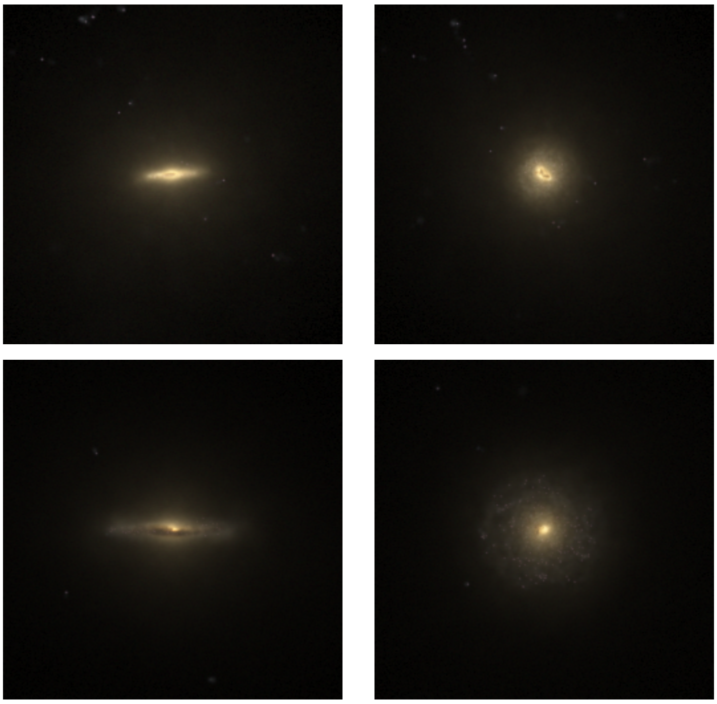

Figure 5. Same as figure 4 for the 2 selected MW-like galaxies in the EAGLE HR run.

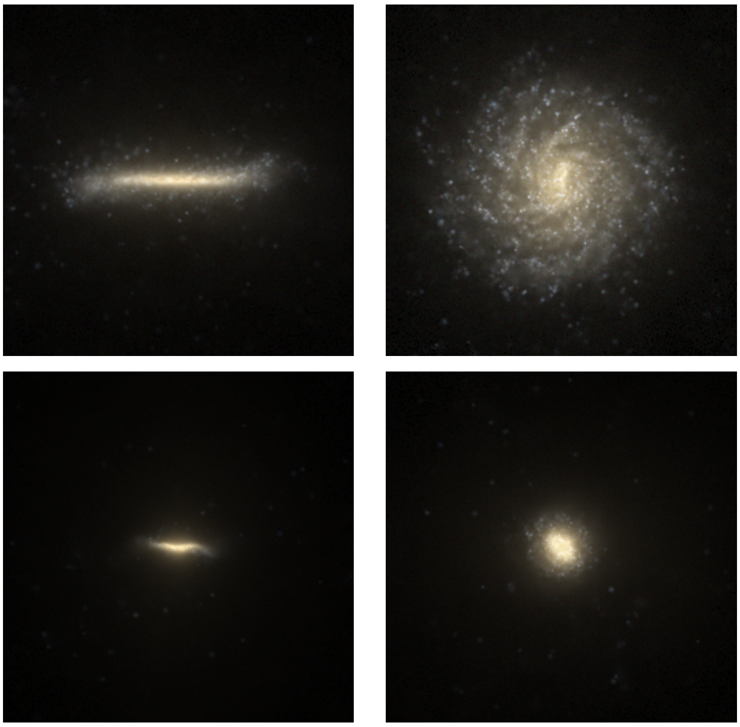

Figure 6. Same as figure 4 for the 2 selected MW-like galaxies in the APOSTLE IR run.

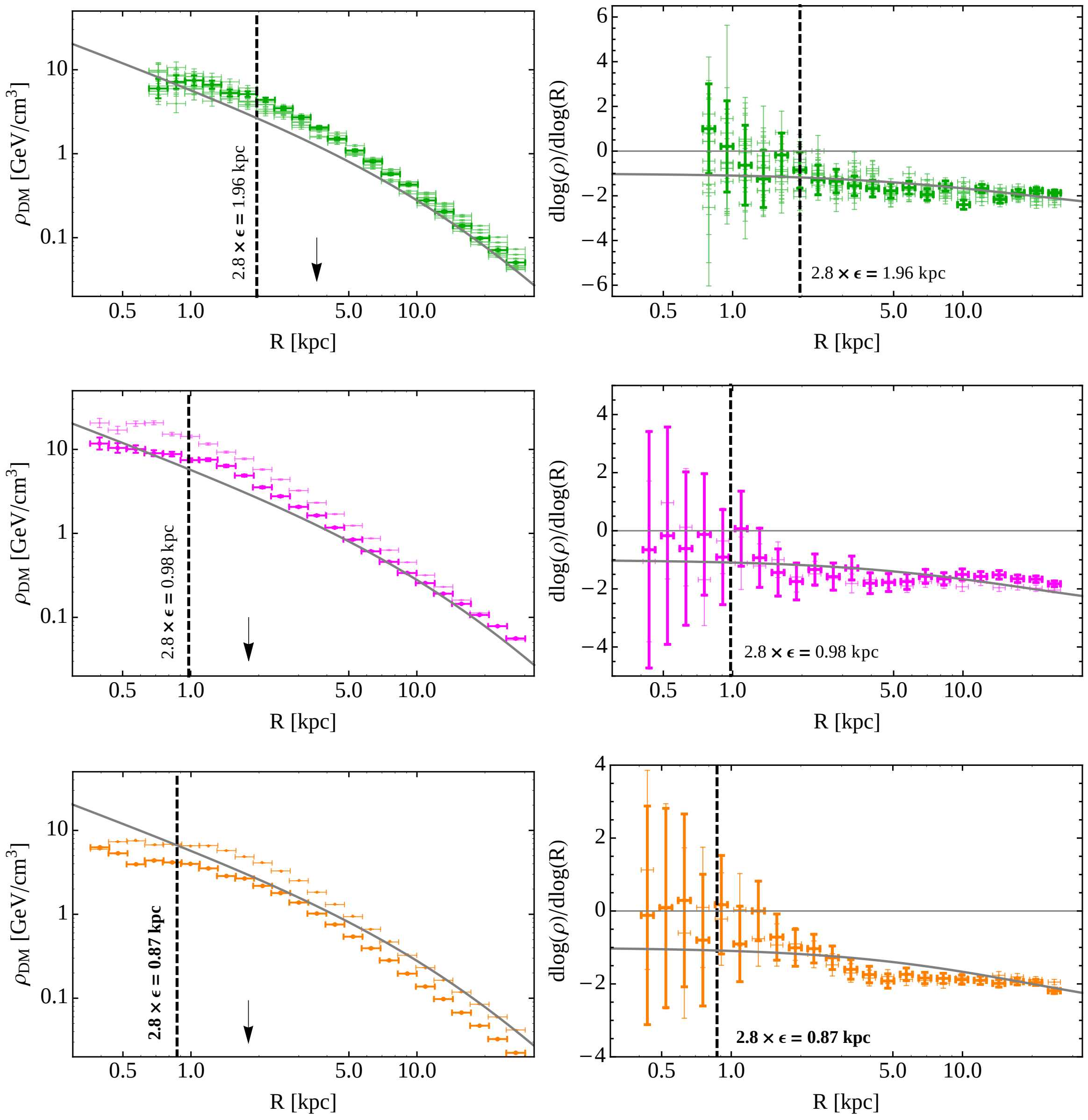

Figure 7. DM density profiles (*left* panels) and the radial change of the local logarithmic slopes (*right* panels) of the selected MW-like galaxies in the EAGLE IR (*top*), EAGLE HR (*middle*) and APOSTLE IR (*bottom*) runs. The *thick grey line* represents the prediction for an NFW profile with $r_s = 20$ kpc and local DM density $\rho_\odot = 0.4$ GeV/cm^3 (as commonly assumed in DM indirect detection studies). In all panels the effective resolution of the simulation is shown by the *dashed black line*, while the *black arrows* on the left panels indicate the convergence radii of 3.6 kpc (EAGLE IR) and 1.8 kpc (EAGLE HR and APOSTLE IR) as discussed in the text.

feature baryon physics, and so the innermost radius at which the profiles may be considered converged is ill-defined. A discussion of these issues can be found in refs. [41, 54, 65].

In figure 7 we show both the resolution limit and the Power radius for the three resolution runs. Between those two radial scales the results of the simulation have to be treated with extreme caution, as there might still be some residual numerical effects due to discreteness and softening of the gravitational force. This is particularly true for the EAGLE IR run, while it is less dramatic for EAGLE HR and APOSTLE IR.

In general, the DM density is shallower than what is expected from an NFW profile in the inner 1.5 – 2 kpc. Between about 1.5 – 6/8 kpc, however, the effect of baryons results in a steeping of the DM profile. Analogous features have been found in the APOSTLE HR simulations [65]. The origin of the flattening in [65] might be related to the star formation history of the haloes: while they developed a cusp at redshifts larger than 1, at $z < 1$ episodes of sudden enhancement of the star formation rate occurred. Such violent starbursts could have destroyed the cusp [10] at sufficiently late times that the galaxy cannot subsequently accrete enough small DM haloes to rebuild the cusp. We stress here that the mild flattening occurring in EAGLE IR between the resolution limit and the Power radius is most likely due to softening effects and limitations in the gas physics model [65], while for EAGLE HR and APOSTLE IR it might be a combination of the softening and of physical effects.

To better appreciate the deviation of the simulated haloes' profiles from pure DM simulations, i.e. from an NFW density profile, in the right panels of figure 7 we show the radial variation of the local logarithmic slope for our selected MW-like galaxies together with the expectation for the NFW density profile. In the case of the EAGLE IR run, it is not possible to establish the presence of the flattening since the error bars on the logarithmic slope make it compatible with the NFW profile down to the resolution limit. This is compatible with what is found by [54], who studied properties of stacked haloes in the EAGLE IR and EAGLE HR simulations. However, for the EAGLE HR and APOSTLE IR selected MW-like galaxies, there is a deviation of the slope from -1 and a tendency to 0 slightly above the resolution limit. From the same panels (EAGLE HR and APOSTLE IR runs) we can also appreciate the effect of the baryonic contraction: in the range 1.5 – 6 kpc the logarithmic slope is steeper than -1.

The two features of the DM profile (flattening below 1.5 kpc and adiabatic contractions below 10 kpc) appear thus to be universal properties of the simulated MW-like galaxies within the EAGLE galaxy formation model, i.e. a generic outcome of the subgrid model assumed. What is striking, though not surprising, is that for the selected MW-like galaxies the overall normalisation of the different DM haloes does not show large scatter. This is again a direct consequence of demanding that the selected galaxies fit the kinematical data of the MW. As a consequence, the variation in the local DM density is also small. For the final sets MW-like galaxies, $\rho_\odot$ (with $R_\odot = 8.0$ kpc) spans the range 0.44 – 0.59 GeV/cm^3 (EAGLE IR), 0.41 – 0.56 GeV/cm^3 (EAGLE HR), and 0.41 GeV/cm^3 (APOSTLE IR). This is compatible with recent measurement of the local DM density, whose standard value at 8.5 kpc is assumed to be 0.4 GeV/cm^3 (which translates to 0.44 GeV/cm^3 at 8.0 kpc) [74, 75]. We acknowledge however that the local DM density is affected by several uncertainties and, in particular, the DM density has been found to be larger in the stellar disc compared to what is derived from a spherical shell [76].

5 The implications for dark matter indirect detection

As explained above, the DM density profile enters squared in the prediction of the gamma-ray intensity flux and anisotropy signal that comes from annihilation of DM particles in the halo of the MW, see for example [77]. Searches for DM at the GC are thus especially sensitive to the uncertainty affecting the determination of the inner distribution of the DM density. In

Profile	$\langle\sigma v\rangle[\times10^{-26}\,\mathrm{cm}^3/\mathrm{s}]$	m_χ [GeV]	χ^2	p-value
gNFW (γ=1.26)	1.71 ± 0.11	47.32 ± 1.07	223.9	0.73
EAGLE HR	1.96 ± 0.14	46.37 ± 1.37	246.3	0.34
APOSTLE IR	1.76 ± 0.16	45.36 ± 2.96	283.9	0.02

Table 3. Best-fit parameters ($\langle\sigma v\rangle$ and mass) together with goodness of fit indicators (χ^2 – with 238 degrees of freedom – and p-value) of the ten sub-regions fit for the gNFW profile, and the best-fit galaxies of the EAGLE HR and APOSTLE IR runs. 100% annihilation into b-quarks is assumed.

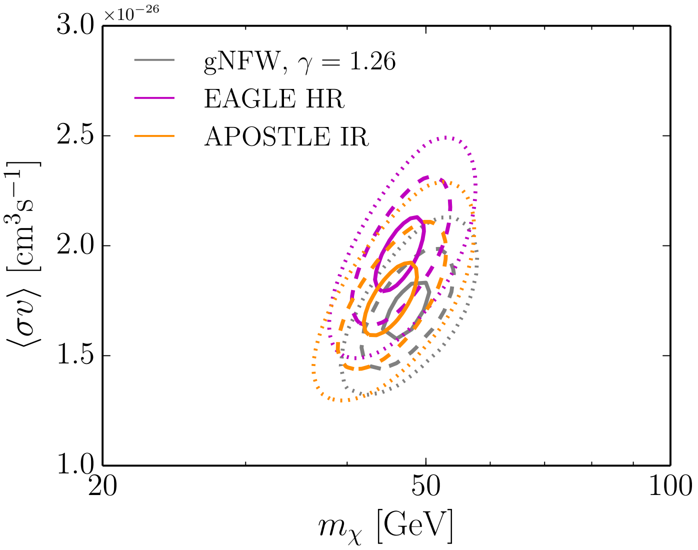

Figure 8. Constraints on the ($\langle\sigma v\rangle$, m_χ) plane for annihilation into b-quarks. The three contours refer to different DM density profiles: the EAGLE HR run best-fit MW-like galaxy's DM density profile (*magenta*), the APOSTLE IR one (*orange*), and the gNFW profile with $\gamma = 1.26$ (*grey*) (cf. table 3).

this section, we focus on the implications that the density profiles discussed above entail for the DM interpretation of the *Fermi* GeV excess.

We remind the reader that the analysis in [25] tested several templates for the GeV excess spatial distribution, i.e. *morphology*, assuming an underlying generalised NFW (gNFW) profile:

$$\rho(r) = \frac{\rho_s}{(r/r_s)^{-\gamma}\,(1 + r/r_s)^{3-\gamma}}\,, \tag{5.1}$$

and varying the inner slope γ in the range 0.7 – 1.5 (thus accounting for both shallower and steeper profiles at small radii than the traditional NFW). The best-fit value of γ was found to be 1.26 ± 0.15, corresponding to an inner slope steeper than the standard NFW profile.

In order to verify the plausibility of this interpretation, it is crucial to test the profiles predicted by hydrodynamic simulations against the GeV excess data. In particular, while we know already that the spectral shape of the signal is compatible with a DM annihilation signal into light and b-quarks pairs (even when properly taking into account the background model systematic uncertainties) [27], the spatial distribution of the signal represents the key-point-test for any model under scrutiny. We use the GeV excess data as derived by [25] in the ten segments analysed in the region $|l| < 2°$ and $2° < |b| < 20°$. This region corresponds to a radial scale from about 0.3 kpc up to 3 kpc. Clearly, the lower limit is not probed by any of our three simulations whose effective resolution, $2.8 \times \epsilon$, is at best 0.87 kpc. Therefore, to make predictions down to the scale at which the GeV excess is measured we need to extrapolate the simulated profiles below the resolution limit.

Following a traditional approach to the extrapolation issue, we adopt a power-law whose steepness is the maximal compatible with the total mass inside the extrapolation radius, namely the maximal asymptotic slope [78, 79]. At each radius r, mean and local densities define a robust upper limit on the asymptotic inner slope: $\gamma_{\rm max}(r) = 3(1 - \rho(r)/\bar{\rho}(r))$. However, as already explained in section 4, possible numerical effects still might occur between the resolution limit and the Power radius. The Power radius was developed for the specific purpose of ascertaining the minimum radius at which the enclosed mass is converged [73], and is a useful guide for this test. For this reason, we believe that only extrapolating from the Power radius guarantees the results to be stable against residual numerical effects. Moreover, we checked that extrapolations from smaller radii (down the the effective resolution limit) would lead to even shallower inner profiles. Given our final aim to compare the simulated DM profiles with the GeV excess data (that require an inner slope as steep as 1.26), our choice is truly "conservative" in a two-fold way: (a) the maximal asymptotic slope extrapolation guarantees that, at any radius r, profiles steeper than the maximal asymptotic slope are not allowed by the simulation data; (b) the choice of the Power radius guarantees that profiles steeper than the maximal asymptotic slope at the Power radius are not allowed by the simulation data *within the resolution/convergence limit of the simulation.*

The profile so determined is the steepest power-law that can be accommodated by the simulation within its resolution/convergence limit.

The maximal asymptotic slope values in the simulation we analysed are:

- EAGLE IR (10 haloes): $0.89 < \gamma_{\rm max} < 1.95$, at $R_{\rm P03}$= 3.6 kpc
- EAGLE HR (2 haloes): $0.94 < \gamma_{\rm max} < 0.98$ at $R_{\rm P03}$= 1.8 kpc
- APOSTLE IR (2 haloes): $0.50 < \gamma_{\rm max} < 0.62$ at $R_{\rm P03}$= 1.8 kpc.

Only among the relatively low-resolution EAGLE IR galaxies we find objects with a maximal slope as steep as the one required to explain the GeV excess emission, 1.26 ± 0.15, and that is only because the maximisation of the slope, if calculated from the relatively large Power radius of 3.6 kpc, leaves considerable freedom in the choice of the profile. For all other DM haloes (of EAGLE IR, EAGLE HR and APOSTLE IR selected MW-like galaxies) the maximal asymptotic slopes at the Power radii are significantly shallower than the steep profile required to fit the data. The result of our extrapolation indicates that no simulated halo has enough DM mass within the Power radius to support profiles as steep as $r^{-1.26}$ (as required by the data). In the following discussion, we will consider *only* high resolution haloes, namely EAGLE HR and APOSTLE IR, since we believe that for those even a very conservative approach might lead to realistic results, contrary to what happens for EAGLE IR, where the resolution is too low to obtain useful constraints.

We adopt the spherically averaged (and extrapolated) DM density profiles of the 4 haloes in EAGLE HR and APOSTLE IR to perform a joint fit in the ten regions analysed by [25]. The aim is to assess how well the GeV excess data are compatible with the spherically symmetric DM signal predicted by EAGLE simulations. The DM signal is the one predicted by the DM density distribution of the 4 selected MW-like galaxies, adopting the maximal asymptotic slope extrapolation. For a generic WIMP DM candidate, the predicted flux of photons is written as:

$$\frac{d\Phi_\gamma}{dE} = \frac{\langle \sigma v \rangle}{8\pi\, m_\chi^2} \frac{dN_\gamma}{dE} \int_{\text{l.o.s.}} ds\; \rho^2(r(s,\psi))\,. \tag{5.2}$$

The particle physics parameters ($\langle \sigma v \rangle$ and mass) are determined by the fitting procedure (see below). The integral along the line of sight (l.o.s.) of the DM density profile squared (which depends on the l.o.s. variable s and on the angle from the GC, ψ), the so-called J-value, instead is fixed for each selected galaxy. We fix the branching ratio to be 100% annihilation into b-quarks (our conclusions are however independent of the assumed annihilation channel) and we compute the corresponding gamma-ray spectrum, dN_γ/dE, with `DarkSUSY 5.1.1` [80]. The fitting procedure fully takes into account the background model systematic uncertainties in each of the ten sub-regions, but it does not account for possible correlations between different sub-regions. The inclusion of those correlated uncertainties has been demonstrated to allow more freedom for models fitting the excess, as thoroughly shown in the case of DM in ref. [27]. The χ^2 function is:

$$\chi^2 = \sum_{i=1}^{10} \sum_{j,k=1}^{24} (d_{ij} - \mu_{ij})(\Sigma^i_{jk})^{-1}(d_{ik} - \mu_{ik})\;, \tag{5.3}$$

where d_{ij} (μ_{ij}) represents the measured (predicted) flux in the segmented region i and energetic bin j; Σ^i_{jk} is the covariance matrix for energy bins j and k in region i [25]. The p-values quoted below refer to this χ^2 function for the ten sub-regions fit, assumed to follow a χ^2_k distribution with $k = 240 - 2$ degrees of freedom.

The free parameters of the fit, $\langle \sigma v \rangle$ and DM mass, are determined by minimising the χ^2 in eq. 5.3. We emphasise that any difference in the absolute normalisation of the DM density profile is re-absorbed in the fitting procedure by a different combination of annihilation cross-section and DM mass that still provides a good fit to the data. The goodness of fit is only determined by the shape of the profile.

In table 3, we quote the best-fit values for $\langle \sigma v \rangle$ and mass, as well as the p-values, for the best-fit galaxies in the EAGLE HR and APOSTLE IR run (and for a gNFW profile with γ=1.26). Correspondingly, we show constraints in the ($\langle \sigma v \rangle$, m_χ) plane from the fit to the ten sub-regions in figure 8. As expected, owing to the lower J-value due to the flattening in the inner kiloparsecs, the best-fit cross section in the case of a DM density profile drawn from the EAGLE HR and APOSTLE IR selected MW-like galaxies is slightly higher than the best-fit cross section obtained when adopting a gNFW ($\gamma = 1.26$) in the fit.[5] Although it has been shown that current upper limits on the annihilation cross section from dwarf spheroidal galaxies are not yet in tension with the DM parameter space preferred by the DM interpretation of the GeV excess when a gNFW profile with $\gamma = 1.26$ is assumed [27], we note that the results obtained by using a shallower DM profile might lead sooner to a tension with dwarf limits.

Figures 9 and 10 show the fluxes in the ten sub-regions for the density profiles of the 4 MW-like galaxies and particle physics parameters as obtained by the fit for each galaxy. In general, all DM haloes of selected galaxies fail in accounting for the flux in the two innermost

---

[5] We note that an additional source of discrepancy in the overall normalisation of the contour regions in figure 8 is due to the different local dark matter density values.

regions, that extend up to 5° (0.75 kpc) above and below the Galactic plane. This is due to the flattening of the profile on scales of $1-2$ kiloparsecs, even when extrapolating the density profile with the maximal asymptotic slope method. On the other hand, in the outermost regions the fit is relatively good because the profile preferred by the data and that used by the model are similar.

In figure 11 we display the angular profile of the DM signal as predicted when using the density profile of the best-fit MW-like galaxies in the EAGLE HR and APOSTLE IR runs. The set of 4 lines refers to the 4 galaxies. For galaxies in the same simulation run the particle physics factor is fixed to the best-fit parameters of the best-fit galaxy of that simulation. The scatter between two lines of the same colour thus indicates the uncertainty affecting the J-value, including the difference in the local DM density. For comparison, the expected DM signal for the gNFW profile with γ=1.26 is also shown. The data point represents the flux of the GeV excess at 5° from the GC. It was demonstrated in [25] that this is a good pivot point since the flux only mildly depends on the inner slope of the DM profile. Below 5° the expected signal from EAGLE HR and APOSTLE IR selected MW-like galaxies does not account for the extra-emission at the GC. The mild discrepancy between all simulated haloes' angular profiles and the gNFW prediction for $R > 2.4$ kpc is due to the different local density normalisation.

Given the DM density profile predicted by the hydrodynamic simulation (and the fact that those profiles are not well described by any of the parameterisations commonly adopted in the literature), we re-analyse *Fermi*-LAT gamma-ray data using a GeV excess template built on the spatial distribution of the galaxy that best fits the GeV excess data, i.e. the best-fit galaxy of the EAGLE HR run. In particular, we are interested in a quantitative estimate of the goodness of fit of such a DM template with respect to the best-fit template adopted in [25]. As thoroughly explained in [25], such an analysis depends on the Galactic diffuse model adopted. We run the fitting template procedure described in [25] for the DM template based on the EAGLE HR DM halo profile *extrapolated* with maximal asymptotic slope at the Power radius of 0.94. We analyse all 60 models for the Galactic diffuse emission presented in [25]. We find that the Galactic diffuse emission model leading to the best fit for the EAGLE HR DM halo template is the so-called model F, the same foreground model giving the best-fit result for a gNFW template with $\gamma = 1.26$. In figure 12, we show the variation of the test statistic[6] TS($= -2\ln\mathcal{L}$), ΔTS, as function of the energy for the best-fit Galactic diffuse model for the EAGLE HR DM halo template when compared to the best-fit one for the gNFW template with $\gamma = 1.26$. The ΔTS is an indicator of how much better a model performs with respect to another at all energies above 1 GeV. It is evident that in general the EAGLE HR DM template leads to a worse fit in the energy range relevant for the GeV excess ($1-3$ GeV), while it performs similarly to the gNFW template at higher energy. To give a term of comparison for the ΔTS values, we show in the same figure the ΔTS between the next-to-best-fit and the best-fit Galactic diffuse emission model when using the gNFW template with $\gamma = 1.26$. The variation in ΔTS due to the different Galactic diffuse emission model are as large as 50, although the differences are more pronounced at low energies. Remarkably, the uncertainties due to the variation of the DM template are comparable to the ones due to the Galactic diffuse modelling.

---

[6] The TS is a measure of the goodness of fit, being directly related to the likelihood.

6 Conclusions

In this work, we have used the set of cosmological, hydrodynamic simulations of the EAGLE [41] and APOSTLE [49] projects. We extracted the simulated haloes in the generous Milky Way-like mass range of $5 \times 10^{11} < M_{200}/\mathrm{M}_\odot < 1 \times 10^{14}$. For each resolution run, we required that the galaxies satisfy observational properties of the Milky Way, besides the uncertain constraint on the halo mass. In particular, we defined galaxies to be *Milky Way-like* if (i) they give a good fit to the Galactic rotation curve [5], (ii) have a stellar mass in the 3σ observed Milky Way stellar mass range [53], and (iii) show a dominant disc in the stellar component. We then analysed the dark matter density profiles of the selected Milky Way-like galaxies and we derived implications for the dark matter interpretation of the *Fermi* GeV excess. We summarise our findings below:

(i) The adopted selection criteria proved to be very powerful in reducing the large variation in the rotation curves predicted by simulated galaxies selected on the basis of the virial mass only (cf. section 3).

(ii) As a consequence, the dark matter density profiles of the Milky Way-like galaxies in our final selection are remarkably consistent with each other, and they have local dark matter densities easily compatible with the measured value of about 0.4 GeV/cm^3.

(iii) The subgrid physics model implemented in EAGLE (and APOSTLE) simulations leads to the dark matter density profiles of Milky Way-like galaxies exhibit a flattening in the inner 1.5 − 2 kpc (probably due to starburst events at low redshift) and a regime of contraction, from 1.5 – 2 kpc up to about 10 kpc, where the profile's slope is steeper than 1. While the flattening in the EAGLE IR simulation might still be affected by numerical effects, the flattening seen in EAGLE HR and APOSTLE IR appears to have a physical origin, cf. section 4.

(iv) We use the dark matter density profiles of the selected Milky Way-like galaxies to compute the predicted gamma-ray flux from dark matter annihilation. We extrapolate the dark matter profiles down to 0.3 kpc through the maximal asymptotic slope method. Even under the very conservative assumption of extrapolating from the Power radius, when performing the fit to the GeV excess data [25], we found that those dark matter profiles fail to reproduce the right morphology of the excess in the innermost regions (within 5° above and below the Galactic plane).[7] On the other hand, all selected Milky Way-like galaxies give a good fit to the GeV excess data in the other regions of interest. Moreover, the parameter space for annihilation cross section and dark matter mass are well in agreement with previous findings within 20%.

We thus showed that the dark matter density profiles of our selected Milky Way-like galaxies lead to a gamma-ray flux from dark matter annihilation in the main Galactic halo that cannot fully account for the observed *Fermi* GeV excess. Our results do not exclude the possibility that dark matter annihilations contribute to the GeV excess, but if that is the case, they require an additional component of emission in the innermost few degrees, e.g. in the form of point-like sources whose fluxes are too dim to be detected by the *Fermi* LAT telescope as individual objects, as recently proposed in Refs. [38, 39].

---

[7] However, we warn the reader that, at the moment, we cannot really rule out that the shallower profile towards the centre is due to numerical or subgrid physics effects [41].

Acknowledgements. We thank Arianna Di Cintio and Cristoph Weniger for useful discussions. Special thanks to Fabio Iocco and Miguel Pato for providing the extensive compilation of rotation curve measurements used in this paper and for many fruitful discussions. G.B. (P.I.), N.B. and F.C. acknowledge support from the European Research Council through the ERC starting grant WIMPs Kairos. This work used the DiRAC Data Centric system at Durham University, operated by the Institute for Computational Cosmology on behalf of the STFC DiRAC HPC Facility (www.dirac.ac.uk). This equipment was funded by BIS National E-infrastructure capital grant ST/K00042X/1, STFC capital grant ST/H008519/1, and STFC DiRAC Operations grant ST/K003267/1 and Durham University. DiRAC is part of the National E-Infrastructure. This work is part of the D-ITP consortium, a program of the Netherlands Organisation for Scientific Research (NWO) that is funded by the Dutch Ministry of Education, Culture and Science (OCW). This work was supported by the Science and Technology Facilities Council (grant number ST/F001166/1); European Research Council (grant numbers GA 267291 "Cosmiway" and GA 278594 "GasAroundGalaxies") and by the Interuniversity Attraction Poles Programme initiated by the Belgian Science Policy Office (AP P7/08 CHARM). R.A.C. is a Royal Society Research Fellow.

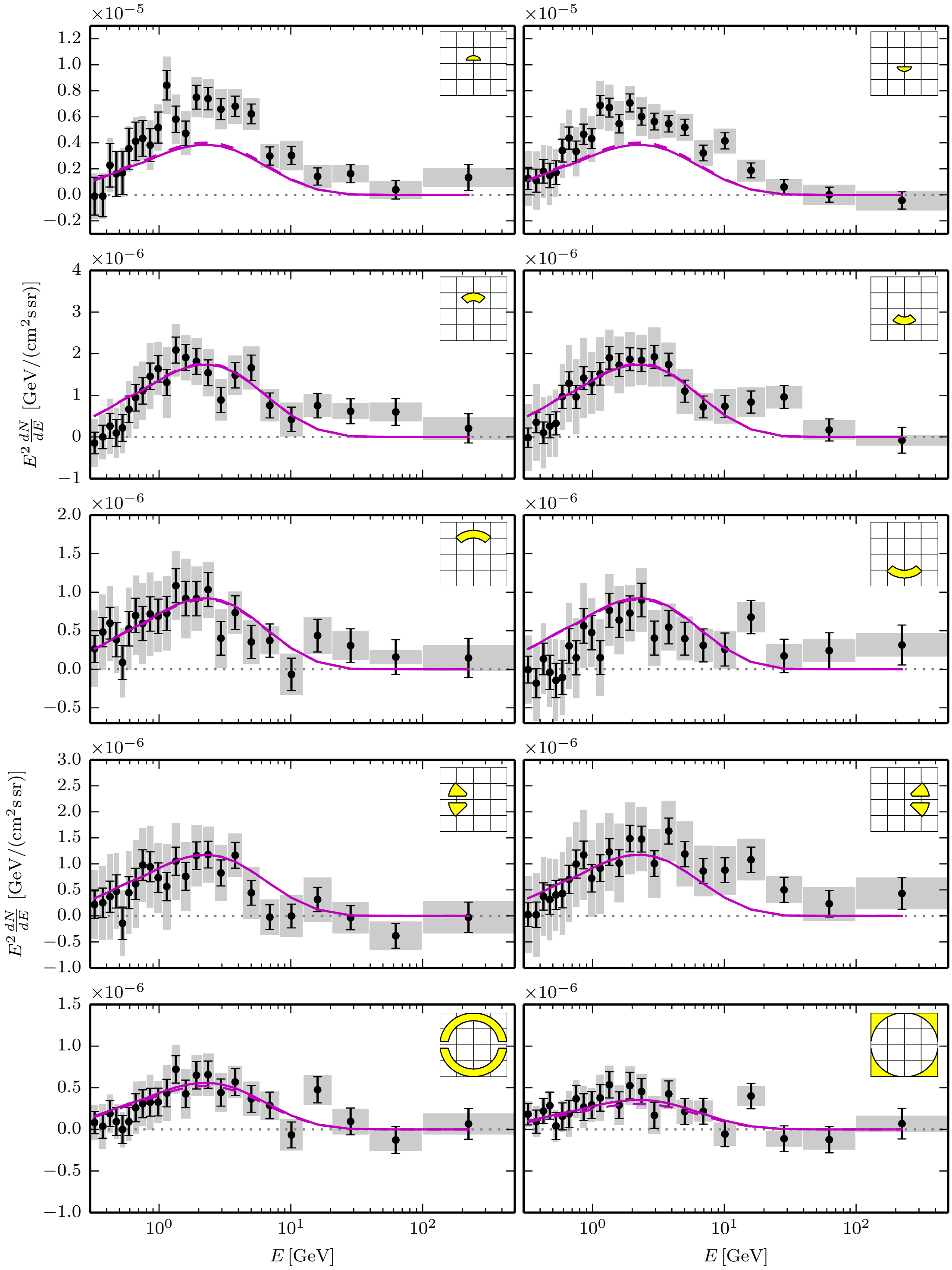

Figure 9. Fluxes in the ten sub-regions for the two MW-like galaxies selected for the EAGLE HR run. The *solid* line indicates the best-fit galaxy, while the *dashed* line corresponds to the other galaxy in the final sample (in most of the regions the two lines overlap because of the fit results). For each galaxy, the flux is computed for mass and cross section as obtained by the fit to the ten sub-regions (see text for details). The *black points* are the GeV excess data as derived in [25], with corresponding systematic uncertainties (*grey boxes*). The insets refer to the region of interest over which the flux is averaged, see [25] for the definition of the ten regions.

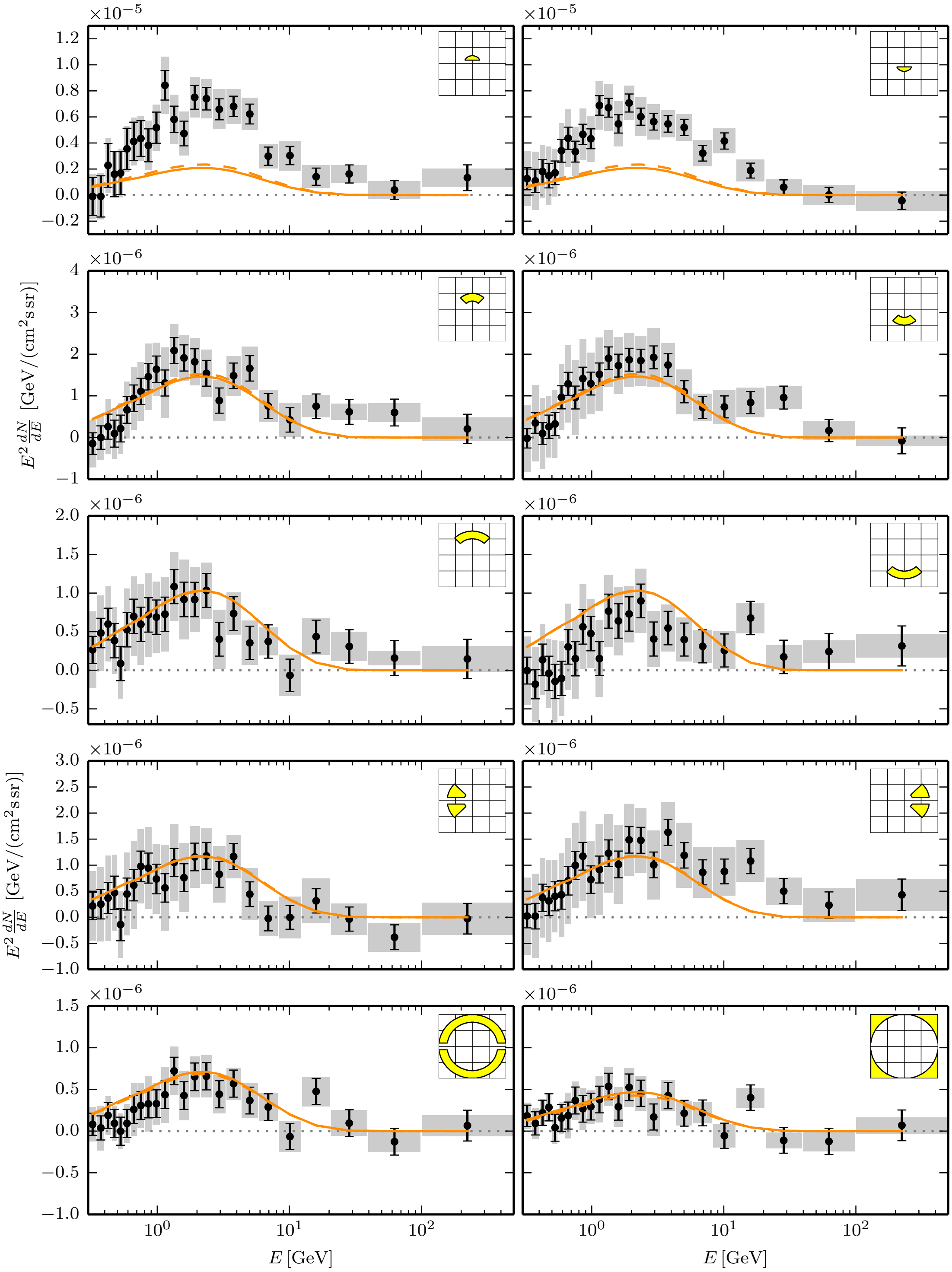

Figure 10. Same as figure 9 for the two MW-like selected haloes in the APOSTLE IR run.

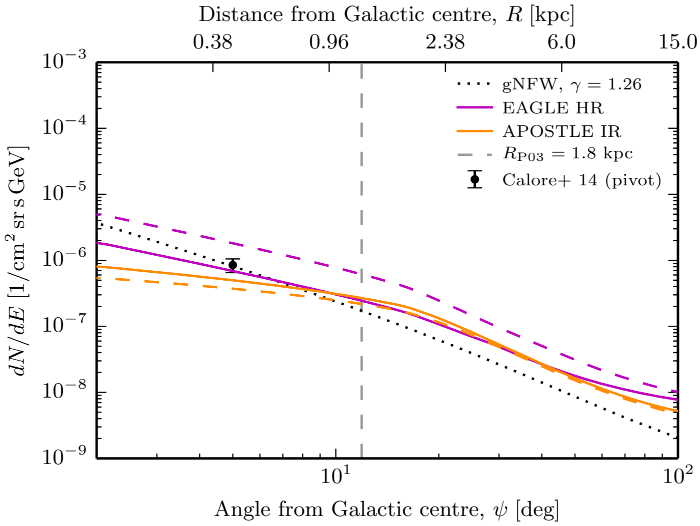

Figure 11. The *magenta* (*orange*) lines represent the angular profile of the DM signal predicted by the selected MW-like halo's density profiles in the EAGLE HR (APOSTLE IR) run. The *solid* line refers to the best-fit halo, while the *dashed* line corresponds to the density profile of the other halo selected normalised to the best-fit cross section and mass of the best-fit halo. The difference between two lines of the same colour thus indicates the uncertainty affecting the J-value. The *black dotted line* represents the expectation for the gNFW profile with γ=1.26 – that best fits the GeV excess data –, while the *black point* is the flux of the GeV excess at 5° away from the GC (that was shown to be a good pivot point in [25]). The *vertical grey dashed* line represents the Power radius for the two simulation runs.

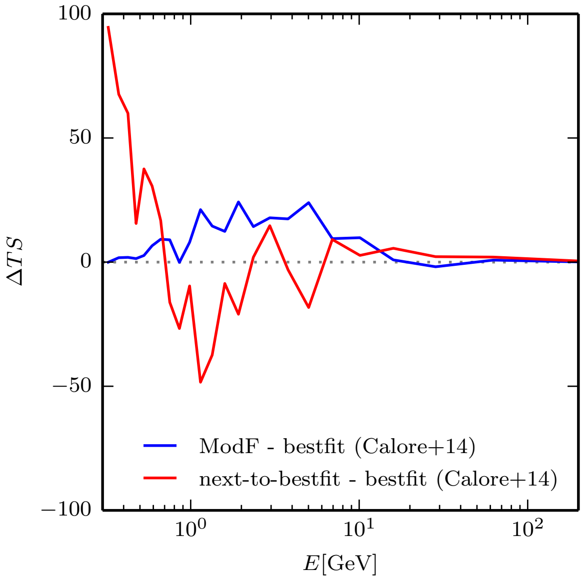

Figure 12. Variation of the TS$(= -2\ln\mathcal{L})$ between the best-fit Galactic diffuse emission model for the EAGLE HR DM profile template and the best-fit Galactic diffuse emission model for the gNFW template [25]: the *blue solid* line uses as DM template the EAGLE HR density profile extrapolated with the maximal asymptotic slope method from the Power radius down to smaller scales. The TS variation of the next-to-best-fit Galactic diffuse emission model for the gNFW template with respect to the best-fit model is shown by the *red line*.

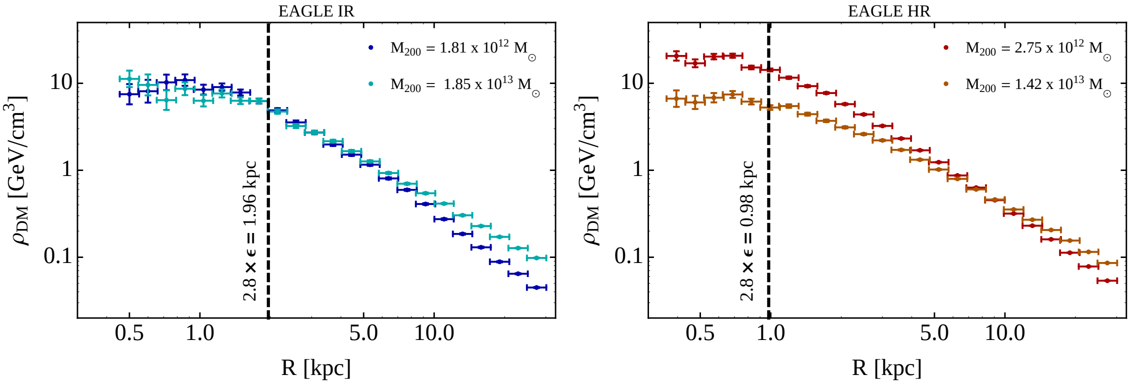

Figure 13. DM density profiles for the two selected haloes with the correct total stellar mass (within 3σ) and with the lowest and largest halo mass, M_{200}, for the EAGLE IR (*left* panel) and EAGLE HR (*right* panel) runs.

A Variation with halo mass

In figure 13, we display the DM density profile for two haloes in the EAGLE IR and EAGLE HR runs that have the correct MW observed stellar mass range (within 3σ) and that have the lowest and highest M_{200} respectively. This figure illustrates that the features of the DM density profile (i.e. the inner flattening and the contraction regime) do not strongly depend on M_{200}. While for EAGLE IR also the normalisation of the density profiles is well matched, for EAGLE HR haloes the overall profile normalisation might differ up to a factor of 5 at the resolution limit. Nevertheless, for the purposes of our analysis, such a normalisation discrepancy is not critical. Indeed, as explained in section. 5, the goodness of fit to the GeV excess data is driven by the shape of the DM density profile in the range $0.3 - 3$ kpc and by the extrapolated maximal asymptotic slope. To demonstrate that the halo mass variation does not introduce any bias in our analysis, we perform the fit to the GeV excess data for the halo with the largest mass in figure 13 (right panel). The best-fit parameters are $\langle \sigma v \rangle = (2.45 \pm 0.20) \times 10^{-26}\,\mathrm{cm}^3/\mathrm{s}$ and $m_\chi = 45.4 \pm 2.1\,\mathrm{GeV}$. Those values are compatible (within 2σ) with the EAGLE HR entry in table 3. In light of this result, we are confident that discrepancies in the halo mass does not alter our final conclusion.

B Varying local Galactic parameters

Throughout this paper, we have assumed $R_0 = 8$ kpc, $v_0 = 230$ km/s, and the peculiar velocity of the Sun, $(U, V, W)_\odot = (11.10, 12.24, 7.25)$ km/s given in Galactic coordinates. In this appendix, we consider different choices of R_0, v_0 and $V_\odot$, showing that the main conclusions of the paper remain unchanged. We follow ref. [81], and consider the following four different configurations:

(a) $R_0 = 7.98$ kpc, $v_0 = 214.44$ km/s for $V_\odot = 26$ km/s;
(b) $R_0 = 7.98$ kpc, $v_0 = 236.94$ km/s for $V_\odot = 5.25$ km/s;
(c) $R_0 = 8.68$ kpc, $v_0 = 235.53$ km/s for $V_\odot = 26$ km/s;
(d) $R_0 = 8.68$ kpc, $v_0 = 258.19$ km/s for $V_\odot = 5.25$ km/s.

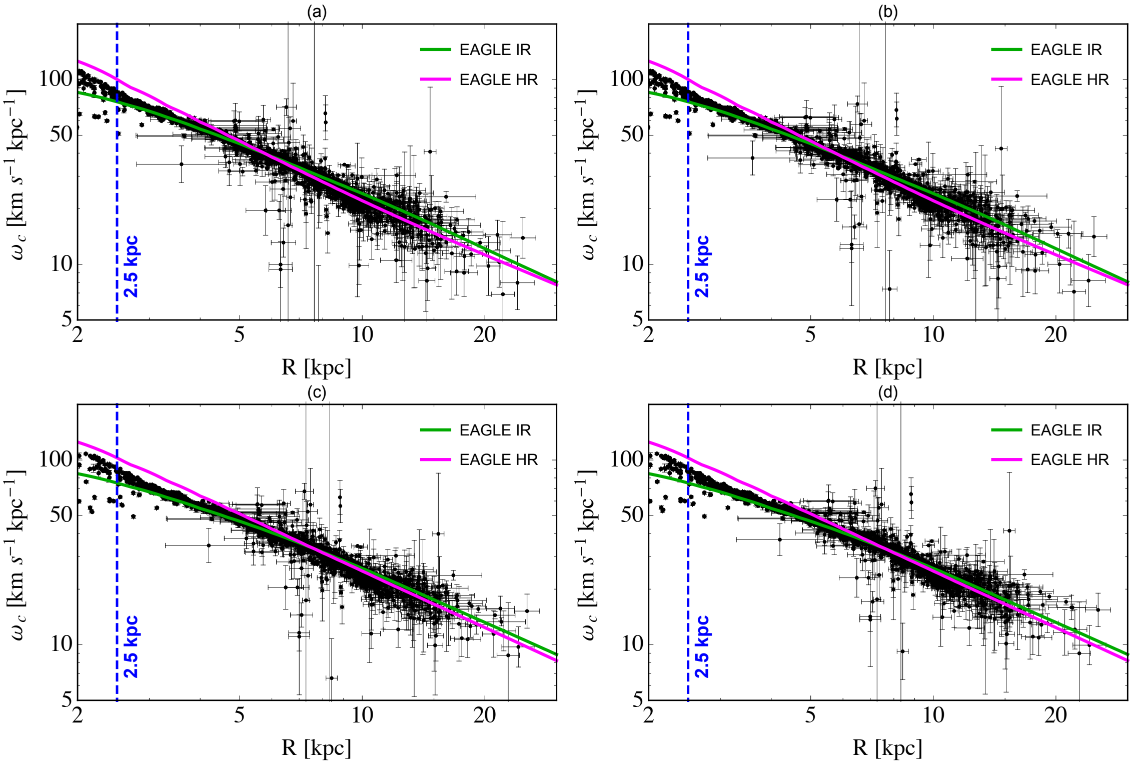

Figure 14. Observed MW angular circular velocity as a function of galactocentric distance from [5] (*black* points and error bars) for configuration (a) (*top left*), (b) (*top right*), (c) (*bottom left*), and (d) (*bottom right*), as well as the best-fit halo in the EAGLE HR (*magenta*) and EAGLE IR (*green*) runs.

Configuration	$\chi^2/(N-1)$, EAGLE HR	$\chi^2/(N-1)$, EAGLE IR
(a)	70.48	15.88
(b)	73.21	16.15
(c)	98.49	16.83
(d)	93.62	17.92

Table 4. Reduced χ^2 values for the best fit haloes which satisfy the criteria in section 3 in the EAGLE HR and EAGLE IR runs for the four configurations discussed in the text.

These configurations are used to obtain the observed MW rotation curve data. We perform the χ^2 analysis discussed in section 3.1 to find the best-fit haloes which satisfy the criteria in section 3. The observational data for the MW angular circular velocity as well as the best-fit haloes for the EAGLE HR and EAGLE IR runs are shown in figure 14. The four panels of the figure correspond to the four configurations. The reduced χ^2 for these haloes are specified in table 4. The DM density profiles of the MW-like selected haloes are shown in figures 15 and 16 for the EAGLE IR and EAGLE HR runs, respectively. All haloes (both in the EAGLE IR and EAGLE HR runs) show a significant deviation from the NFW profile and the common features of the density profile discussed in section 4 can be found also when varying R_0, v_0 and $V_\odot$ parameters.

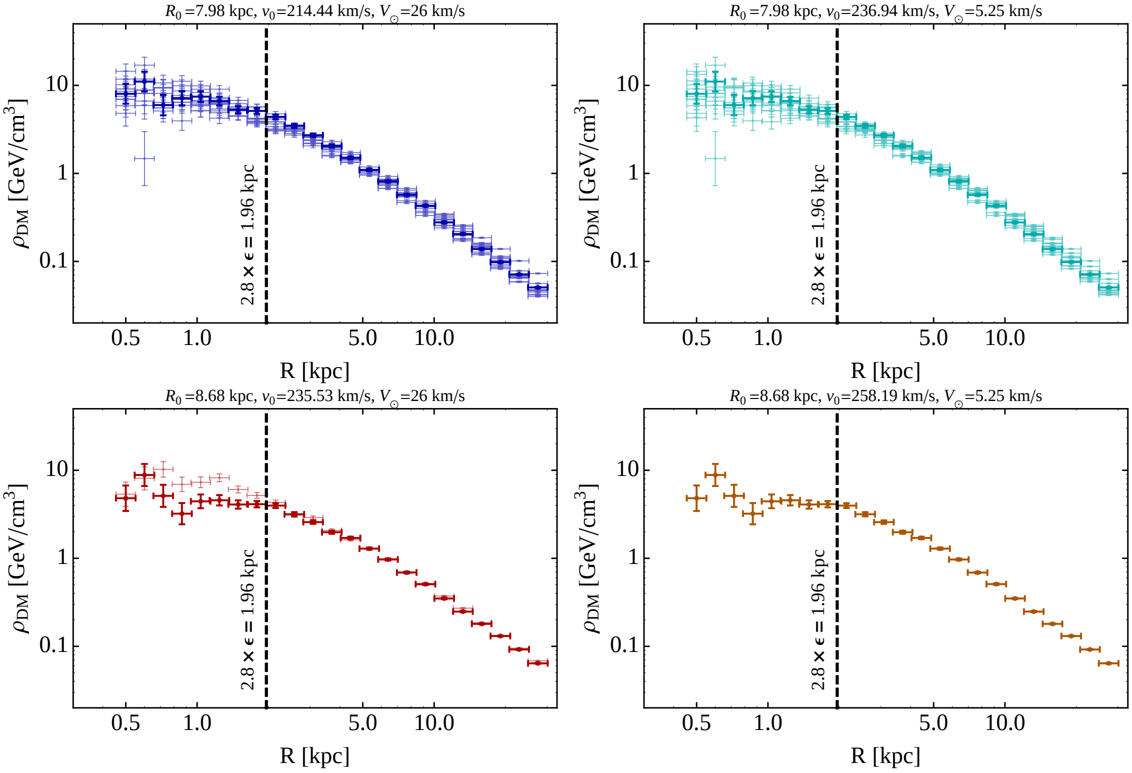

Figure 15. Same as figure 7 for the EAGLE IR run and for the four combinations of v_0 and R_0.

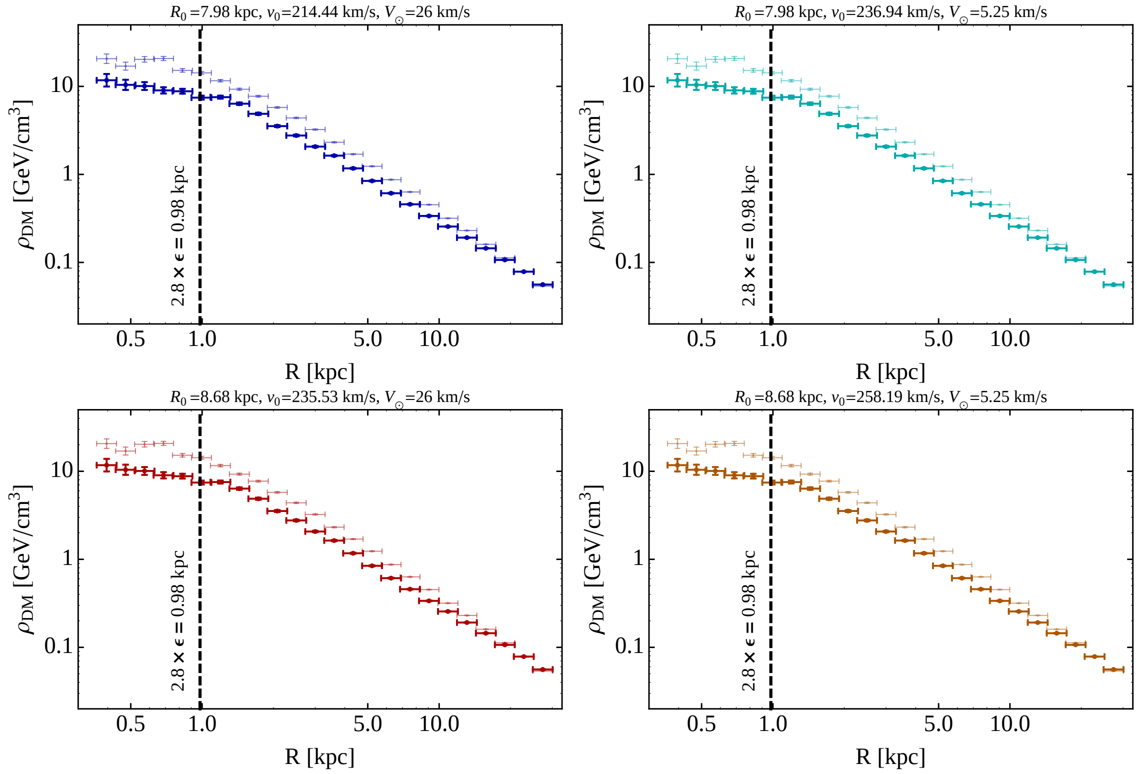

Figure 16. Same as figure 7 for the EAGLE HR run and for the four combinations of v_0 and R_0.

References

[1] G. Bertone, ed., *Particle Dark Matter: Observations, Models and Searches*. Cambridge U. Press, 2010.

[2] G. Jungman, M. Kamionkowski, and K. Griest, *Supersymmetric dark matter*, *Phys.Rept.* **267** (1996) 195–373, [hep-ph/9506380].

[3] L. Bergström, *Non-baryonic dark matter: observational evidence and detection methods*, *Rep. Prog. Phys.* **63** (2000) 793–841, [hep-ph/0002126].

[4] G. Bertone, D. Hooper, and J. Silk, *Particle dark matter: Evidence, candidates and constraints*, *Phys.Rept.* **405** (2005) 279–390, [hep-ph/0404175].

[5] F. Iocco, M. Pato, and G. Bertone, *Evidence for dark matter in the inner Milky Way*, arXiv:1502.03821.

[6] M. Pato, F. Iocco, and G. Bertone, *Dynamical constraints on the dark matter distribution in the Milky Way*, *ArXiv e-prints* (Apr., 2015) [arXiv:1504.06324].

[7] M. Pato and F. Iocco, *The Dark Matter Profile of the Milky Way: A Non-parametric Reconstruction*, ApJ **803** (Apr., 2015) L3, [arXiv:1504.03317].

[8] P. Salucci, A. Lapi, C. Tonini, G. Gentile, I. Yegorova, and U. Klein, *The universal rotation curve of spiral galaxies - II. The dark matter distribution out to the virial radius*, MNRAS **378** (June, 2007) 41–47, [astro-ph/0703115].

[9] J. F. Navarro, C. S. Frenk, and S. D. White, *A Universal density profile from hierarchical clustering*, *Astrophys.J.* **490** (1997) 493–508, [astro-ph/9611107].

[10] J. F. Navarro, V. R. Eke, and C. S. Frenk, *The cores of dwarf galaxy halos*, *Mon.Not.Roy.Astron.Soc.* **283** (1996) L72–L78, [astro-ph/9610187].

[11] M. D. Weinberg and N. Katz, *Bar-driven dark halo evolution: a resolution of the cusp-core controversy*, *Astrophys.J.* **580** (2002) 627–633, [astro-ph/0110632].

[12] S. Mashchenko, H. Couchman, and J. Wadsley, *Cosmological puzzle resolved by stellar feedback in high redshift galaxies*, *Nature* **442** (2006) 539, [astro-ph/0605672].

[13] A. Pontzen and F. Governato, *How supernova feedback turns dark matter cusps into cores*, *Mon.Not.Roy.Astron.Soc.* **421** (2012) 3464, [arXiv:1106.0499].

[14] P. Mollitor, E. Nezri, and R. Teyssier, *Baryonic and dark matter distribution in cosmological simulations of spiral galaxies*, *Mon.Not.Roy.Astron.Soc.* **447** (2015), no. 2 1353–1369, [arXiv:1405.4318].

[15] G. R. Blumenthal, S. Faber, R. Flores, and J. R. Primack, *Contraction of Dark Matter Galactic Halos Due to Baryonic Infall*, *Astrophys.J.* **301** (1986) 27.

[16] O. Y. Gnedin, A. V. Kravtsov, A. A. Klypin, and D. Nagai, *Response of dark matter halos to condensation of baryons: Cosmological simulations and improved adiabatic contraction model*, *Astrophys.J.* **616** (2004) 16–26, [astro-ph/0406247].

[17] L. Goodenough and D. Hooper, *Possible Evidence For Dark Matter Annihilation In The Inner Milky Way From The Fermi Gamma Ray Space Telescope*, arXiv:0910.2998.

[18] D. Hooper and L. Goodenough, *Dark Matter Annihilation in The Galactic Center As Seen by the Fermi Gamma Ray Space Telescope*, *Phys.Lett.* **B697** (2011) 412–428, [arXiv:1010.2752].

[19] D. Hooper and T. Linden, *On The Origin Of The Gamma Rays From The Galactic Center*, *Phys.Rev.* **D84** (2011) 123005, [arXiv:1110.0006].

[20] K. N. Abazajian and M. Kaplinghat, *Detection of a Gamma-Ray Source in the Galactic Center Consistent with Extended Emission from Dark Matter Annihilation and Concentrated*

Astrophysical Emission, *Phys.Rev.* **D86** (2012) 083511, [arXiv:1207.6047].

[21] C. Gordon and O. Macias, *Dark Matter and Pulsar Model Constraints from Galactic Center Fermi-LAT Gamma Ray Observations*, *Phys.Rev.* **D88** (2013) 083521, [arXiv:1306.5725].

[22] D. Hooper and T. R. Slatyer, *Two Emission Mechanisms in the Fermi Bubbles: A Possible Signal of Annihilating Dark Matter*, *Phys.Dark Univ.* **2** (2013) 118–138, [arXiv:1302.6589].

[23] K. N. Abazajian, N. Canac, S. Horiuchi, and M. Kaplinghat, *Astrophysical and Dark Matter Interpretations of Extended Gamma-Ray Emission from the Galactic Center*, *Phys.Rev.* **D90** (2014), no. 2 023526, [arXiv:1402.4090].

[24] T. Daylan, D. P. Finkbeiner, D. Hooper, T. Linden, S. K. N. Portillo, et al., *The Characterization of the Gamma-Ray Signal from the Central Milky Way: A Compelling Case for Annihilating Dark Matter*, arXiv:1402.6703.

[25] F. Calore, I. Cholis, and C. Weniger, *Background model systematics for the Fermi GeV excess*, *JCAP* **1503** (2015) 038, [arXiv:1409.0042].

[26] **Fermi-LAT** Collaboration, S. Murgia, *Observations of High-Energy Gamma-Ray Emission Toward the Galactic Center*, *Talk given at the 2014 Fermi Symposium, Nagoya, Japan, October 20-24* (2014).

[27] F. Calore, I. Cholis, C. McCabe, and C. Weniger, *A Tale of Tails: Dark Matter Interpretations of the Fermi GeV Excess in Light of Background Model Systematics*, arXiv:1411.4647.

[28] A. Achterberg, S. Caron, L. Hendriks, R. Ruiz de Austri, and C. Weniger, *A description of the Galactic Center excess in the Minimal Supersymmetric Standard Model*, arXiv:1502.05703.

[29] D. Hooper, I. Cholis, T. Linden, J. Siegal-Gaskins, and T. Slatyer, *Millisecond pulsars Cannot Account for the Inner Galaxy's GeV Excess*, *Phys.Rev.* **D88** (2013) 083009, [arXiv:1305.0830].

[30] I. Cholis, D. Hooper, and T. Linden, *Challenges in Explaining the Galactic Center Gamma-Ray Excess with Millisecond Pulsars*, arXiv:1407.5625.

[31] J. Petrovic, P. D. Serpico, and G. Zaharijas, *Millisecond pulsars and the Galactic Center gamma-ray excess: the importance of luminosity function and secondary emission*, arXiv:1411.2980.

[32] Q. Yuan and B. Zhang, *Millisecond pulsar interpretation of the Galactic center gamma-ray excess*, arXiv:1404.2318.

[33] R. M. O'Leary, M. D. Kistler, M. Kerr, and J. Dexter, *Young Pulsars and the Galactic Center GeV Gamma-ray Excess*, arXiv:1504.02477.

[34] E. Carlson and S. Profumo, *Cosmic Ray Protons in the Inner Galaxy and the Galactic Center Gamma-Ray Excess*, *Phys.Rev.* **D90** (2014) 023015, [arXiv:1405.7685].

[35] J. Petrovic, P. D. Serpico, and G. Zaharijas, *Galactic Center gamma-ray "excess" from an active past of the Galactic Centre?*, *JCAP* **1410** (2014), no. 10 052, [arXiv:1405.7928].

[36] I. Cholis, C. Evoli, F. Calore, T. Linden, C. Weniger, and D. Hooper, *The Galactic Center GeV Excess from a Series of Leptonic Cosmic-Ray Outbursts*, *To be submitted to JCAP* (2015) [arXiv:1506.05119].

[37] D. Gaggero, M. Taoso, A. Urbano, M. Valli, and P. Ullio, *Towards a realistic astrophysical interpretation of the Galactic center excess*, arXiv:1507.06129.

[38] S. K. Lee, M. Lisanti, B. R. Safdi, T. R. Slatyer, and W. Xue, *Evidence for Unresolved Gamma-Ray Point Sources in the Inner Galaxy*, arXiv:1506.05124.

[39] R. Bartels, S. Krishnamurthy, and C. Weniger, *Strong support for the millisecond pulsar origin of the Galactic center GeV excess*, arXiv:1506.05104.

[40] F. Calore, M. Di Mauro, and F. Donato, *Diffuse gamma-ray emission from galactic pulsars*,

Astrophys.J. **796** (2014) 1, [arXiv:1406.2706].

[41] J. Schaye, R. A. Crain, R. G. Bower, M. Furlong, M. Schaller, T. Theuns, C. Dalla Vecchia, C. S. Frenk, I. G. McCarthy, J. C. Helly, A. Jenkins, Y. M. Rosas-Guevara, S. D. M. White, M. Baes, C. M. Booth, P. Camps, J. F. Navarro, Y. Qu, A. Rahmati, T. Sawala, P. A. Thomas, and J. Trayford, *The EAGLE project: simulating the evolution and assembly of galaxies and their environments*, MNRAS **446** (Jan., 2015) 521–554, [arXiv:1407.7040].

[42] R. A. Crain, J. Schaye, R. G. Bower, M. Furlong, M. Schaller, T. Theuns, C. Dalla Vecchia, C. S. Frenk, I. G. McCarthy, J. C. Helly, A. Jenkins, Y. M. Rosas-Guevara, S. D. M. White, and J. W. Trayford, *The EAGLE simulations of galaxy formation: calibration of subgrid physics and model variations*, MNRAS **450** (June, 2015) 1937–1961, [arXiv:1501.01311].

[43] N. Bozorgnia, F. Calore, G. Bertone, M. Lovell, M. Schaller, et al., *Simulated Milky Way analogues: implications for dark matter direct detection*, *In preparation for JCAP* (2015).

[44] V. Springel, J. Wang, M. Vogelsberger, A. Ludlow, A. Jenkins, A. Helmi, J. F. Navarro, C. S. Frenk, and S. D. M. White, *The Aquarius Project: the subhaloes of galactic haloes*, MNRAS **391** (2008) 1685–1711.

[45] P. F. Hopkins, *A general class of Lagrangian smoothed particle hydrodynamics methods and implications for fluid mixing problems*, MNRAS **428** (Feb., 2013) 2840–2856, [arXiv:1206.5006].

[46] M. Schaller, C. Dalla Vecchia, J. Schaye, R. G. Bower, T. Theuns, R. A. Crain, M. Furlong, and I. G. McCarthy, *The EAGLE simulations of galaxy formation: the importance of the hydrodynamics scheme*, MNRAS **454** (Dec., 2015) 2277–2291, [arXiv:1509.05056].

[47] Planck Collaboration, P. A. R. Ade, N. Aghanim, C. Armitage-Caplan, M. Arnaud, M. Ashdown, F. Atrio-Barandela, J. Aumont, C. Baccigalupi, A. J. Banday, and et al., *Planck 2013 results. XVI. Cosmological parameters*, A&A **571** (Nov., 2014) A16, [arXiv:1303.5076].

[48] R. C. Kennicutt, Jr., *The Global Schmidt Law in Star-forming Galaxies*, *ApJ* **498** (May, 1998) 541, [astro-ph/9712213].

[49] T. Sawala, C. S. Frenk, A. Fattahi, J. F. Navarro, R. G. Bower, R. A. Crain, C. Dalla Vecchia, M. Furlong, J. C. Helly, A. Jenkins, K. A. Oman, M. Schaller, J. Schaye, T. Theuns, J. Trayford, and S. D. M. White, *The APOSTLE simulations: solutions to the Local Group's cosmic puzzles*, *ArXiv e-prints* (Nov., 2015) [arXiv:1511.01098].

[50] A. Fattahi, J. F. Navarro, T. Sawala, C. S. Frenk, K. A. Oman, R. A. Crain, M. Furlong, M. Schaller, J. Schaye, T. Theuns, and A. Jenkins, *The APOSTLE project: Local Group kinematic mass constraints and simulation candidate selection*, *ArXiv e-prints* (July, 2015) [arXiv:1507.03643].

[51] V. Springel, S. D. M. White, G. Tormen, and G. Kauffmann, *Populating a cluster of galaxies - I. Results at [formmu2]z=0*, *MNRAS* **328** (Dec., 2001) 726–750, [astro-ph/0012055].

[52] P. S. Behroozi, R. H. Wechsler, and C. Conroy, *The Average Star Formation Histories of Galaxies in Dark Matter Halos from z = 0-8*, *Astrophys.J.* **770** (June, 2013) 57, [arXiv:1207.6105].

[53] P. J. McMillan, *Mass models of the Milky Way*, *Mon.Not.Roy.Astron.Soc.* **414** (2011) 2446–2457, [arXiv:1102.4340].

[54] M. Schaller, C. S. Frenk, R. G. Bower, T. Theuns, A. Jenkins, J. Schaye, R. A. Crain, M. Furlong, C. Dalla Vecchia, and I. G. McCarthy, *Baryon effects on the internal structure of ΛCDM haloes in the EAGLE simulations*, MNRAS **451** (Aug., 2015) 1247–1267, [arXiv:1409.8617].

[55] R. Schönrich, J. Binney, and W. Dehnen, *Local kinematics and the local standard of rest*, MNRAS **403** (Apr., 2010) 1829–1833, [arXiv:0912.3693].

[56] M. T. Busha, P. J. Marshall, R. H. Wechsler, A. Klypin, and J. Primack, *The Mass Distribution and Assembly of the Milky Way from the Properties of the Magellanic Clouds*, *Astrophys.J.* **743** (2011) 40, [arXiv:1011.2203].

[57] P. J. E. Peebles, R. B. Tully, and E. J. Shaya, *A Dynamical Model of the Local Group*, *ArXiv e-prints* (May, 2011) [arXiv:1105.5596].

[58] P. S. Behroozi, D. Marchesini, R. H. Wechsler, A. Muzzin, C. Papovich, and M. Stefanon, *Using Cumulative Number Densities to Compare Galaxies across Cosmic Time*, ApJ **777** (Nov., 2013) L10, [arXiv:1308.3232].

[59] J. E. Forero-Romero, Y. Hoffman, S. Bustamante, S. Gottlöber, and G. Yepes, *The Kinematics of the Local Group in a Cosmological Context*, ApJ **767** (Apr., 2013) L5, [arXiv:1303.2690].

[60] C. Barber, E. Starkenburg, J. F. Navarro, A. W. McConnachie, and A. Fattahi, *The orbital ellipticity of satellite galaxies and the mass of the Milky Way*, MNRAS **437** (Jan., 2014) 959–967, [arXiv:1310.0466].

[61] C. Scannapieco, S. D. White, V. Springel, and P. B. Tissera, *The Formation and Survival of Discs in a Lambda-CDM Universe*, *Mon.Not.Roy.Astron.Soc.* **396** (2009) 696, [arXiv:0812.0976].

[62] C. Scannapieco, M. Wadepuhl, O. Parry, J. Navarro, A. Jenkins, et al., *The Aquila comparison Project: The Effects of Feedback and Numerical Methods on Simulations of Galaxy Formation*, *Mon.Not.Roy.Astron.Soc.* **423** (2012) 1726, [arXiv:1112.0315].

[63] L. V. Sales, J. F. Navarro, T. Theuns, J. Schaye, S. D. M. White, C. S. Frenk, R. A. Crain, and C. Dalla Vecchia, *The origin of discs and spheroids in simulated galaxies*, MNRAS **423** (June, 2012) 1544–1555, [arXiv:1112.2220].

[64] C. Scannapieco, D. A. Gadotti, P. Jonsson, and S. D. White, *An observer's view of simulated galaxies: disc-to-total ratios, bars, and (pseudo-)bulges*, *Mon.Not.Roy.Astron.Soc.* **407** (2010) 41, [arXiv:1001.4890].

[65] M. Schaller, C. S. Frenk, T. Theuns, F. Calore, G. Bertone, N. Bozorgnia, R. A. Crain, A. Fattahi, J. F. Navarro, T. Sawala, and J. Schaye, *Dark matter annihilation radiation in hydrodynamic simulations of Milky Way haloes*, *ArXiv e-prints* (Sept., 2015) [arXiv:1509.02166].

[66] P. Camps and M. Baes, *SKIRT: An advanced dust radiative transfer code with a user-friendly architecture*, *Astronomy and Computing* **9** (Mar., 2015) 20–33, [arXiv:1410.1629].

[67] J. W. Trayford, T. Theuns, R. G. Bower, J. Schaye, M. Furlong, M. Schaller, C. S. Frenk, R. A. Crain, C. D. Vecchia, and I. G. McCarthy, *Colours and luminosities of $z = 0.1$ galaxies in the EAGLE simulation*, MNRAS **452** (Sept., 2015) 2879–2896, [arXiv:1504.04374].

[68] J. W. Trayford et al., *In preparation*, .

[69] A. W. Graham and C. Worley, *Inclination- and dust-corrected galaxy parameters: Bulge-to-disc ratios and size-luminosity relations*, *Mon.Not.Roy.Astron.Soc.* **388** (2008) 1708, [arXiv:0805.3565].

[70] J. Dubinski, *The effect of dissipation on the shapes of dark halos*, *Astrophys.J.* **431** (Aug., 1994) 617–624, [astro-ph/9309001].

[71] S. E. Bryan, S. T. Kay, A. R. Duffy, J. Schaye, C. Dalla Vecchia, and C. M. Booth, *The impact of baryons on the spins and shapes of dark matter haloes*, MNRAS **429** (Mar., 2013) 3316–3329, [arXiv:1207.4555].

[72] N. Bernal, J. E. Forero-Romero, R. Garani, and S. Palomares-Ruiz, *Systematic uncertainties from halo asphericity in dark matter searches*, *JCAP* **1409** (2014) 004, [arXiv:1405.6240].

[73] C. Power, J. Navarro, A. Jenkins, C. Frenk, S. D. White, et al., *The Inner structure of Lambda*

CDM halos. 1. A Numerical convergence study, *Mon.Not.Roy.Astron.Soc.* **338** (2003) 14–34, [astro-ph/0201544].

[74] R. Catena and P. Ullio, *A novel determination of the local dark matter density*, *JCAP* **1008** (2010) 004, [arXiv:0907.0018].

[75] P. Salucci, F. Nesti, G. Gentile, and C. Frigerio Martins, *The dark matter density at the Sun's location*, A&A **523** (Nov., 2010) A83, [arXiv:1003.3101].

[76] M. Pato, O. Agertz, G. Bertone, B. Moore, and R. Teyssier, *Systematic uncertainties in the determination of the local dark matter density*, *Phys.Rev.* **D82** (2010) 023531, [arXiv:1006.1322].

[77] F. Calore, V. De Romeri, M. Di Mauro, F. Donato, J. Herpich, A. V. Macci, and L. Maccione, *γ-ray anisotropies from dark matter in the Milky Way: the role of the radial distribution*, *Mon. Not. Roy. Astron. Soc.* **442** (2014), no. 2 1151–1156, [arXiv:1402.0512].

[78] J. F. Navarro, E. Hayashi, C. Power, A. R. Jenkins, C. S. Frenk, S. D. M. White, V. Springel, J. Stadel, and T. R. Quinn, *The inner structure of ΛCDM haloes - III. Universality and asymptotic slopes*, MNRAS **349** (Apr., 2004) 1039–1051, [astro-ph/0311231].

[79] V. Springel, J. Wang, M. Vogelsberger, A. Ludlow, A. Jenkins, A. Helmi, J. F. Navarro, C. S. Frenk, and S. D. M. White, *The Aquarius Project: the subhalos of galactic halos*, *Mon. Not. Roy. Astron. Soc.* **391** (2008) 1685–1711, [arXiv:0809.0898].

[80] P. Gondolo, J. Edsjo, P. Ullio, L. Bergstrom, M. Schelke, et al., *DarkSUSY: Computing supersymmetric dark matter properties numerically*, *JCAP* **0407** (2004) 008, [astro-ph/0406204].

[81] F. Iocco, M. Pato, and G. Bertone, *Testing modified Newtonian dynamics in the Milky Way*, arXiv:1505.05181.